Java–Sumatra Niño/Niña and Its Impact on Regional Rainfall Variability

SANG-KI LEE,[a] HOSMAY LOPEZ,[a] GREGORY R. FOLTZ,[a] EUN-PA LIM,[b] DONGMIN KIM,[c,a] SARAH M. LARSON,[d] KANDAGA PUJIANA,[c,a] DENIS L. VOLKOV,[c,a] SOUMI CHAKRAVORTY,[c,a] AND FABIAN A. GOMEZ[e,a]

[a] *NOAA/Atlantic Oceanographic and Meteorological Laboratory, Miami, Florida*
[b] *Bureau of Meteorology, Melbourne, Victoria, Australia*
[c] *Cooperative Institute for Marine and Atmospheric Studies, University of Miami, Miami, Florida*
[d] *Marine, Earth, and Atmospheric Sciences, North Carolina State University, Raleigh, North Carolina*
[e] *Northern Gulf Institute, Mississippi State University, Mississippi State, Mississippi*

(Manuscript received 13 August 2021, in final form 5 March 2022)

ABSTRACT: A phenomenon referred to here as Java–Sumatra Niño/Niña (JSN or JS Niño/Niña) is characterized by the appearance of warm/cold sea surface temperature anomalies (SSTAs) in the coastal upwelling region off Java–Sumatra in the southeastern equatorial Indian Ocean. JSN develops in July–September and sometimes as a precursor to the Indian Ocean dipole, but often without corresponding SSTAs in the western equatorial Indian Ocean. Although its spatiotemporal evolution varies considerably between individual events, JSN is essentially an intrinsic mode of variability driven by local atmosphere–ocean positive feedback, and thus does not rely on remote forcing from the Pacific for its emergence. JSN is an important driver of climate variability over the tropical Indian Ocean and the surrounding continents. Notably, JS Niña events developing in July–September project onto the South and Southeast Asian summer monsoons, increasing the probability of heavy rainfall and flooding across the most heavily populated regions of the world.

KEYWORDS: Indian Ocean; Atmosphere-ocean interaction; El Nino; ENSO; La Nina; Ocean dynamics; Teleconnections; Rainfall; Climate variability; Interannual variability; Oceanic variability; Tropical variability

1. Introduction

In boreal fall [September–November (SON)], sea surface temperature anomalies (SSTAs) in the tropical Indian Ocean are often characterized by the Indian Ocean dipole (IOD), a key driver of rainfall variability in Southeast Asia, southeastern Australia, and eastern Africa (e.g., Saji et al. 1999; Webster et al. 1999; Ashok et al. 2001, 2004; England et al. 2006; Meyers et al. 2007; Risbey et al. 2009; Sreelekha and Babu 2019). The anomalous SST gradient from the southeastern equatorial Indian Ocean (90°–110°E and 10°S–0°) to the western equatorial Indian Ocean (50°–70°E and 10°S–10°N), which is referred to as the dipole mode index (DMI; Saji et al. 1999), has been widely used to represent the occurrence and intensity of IOD events. However, the propriety of "dipole" in Saji et al. (1999) has been debated intensely in multiple studies because SSTAs in the western and southeastern equatorial regions are poorly correlated (Allan et al. 2001; Hastenrath 2002; Yamagata et al. 2003; Dommenget 2011; Zhao and Nigam 2015). Indeed, on interannual time scales, the correlation coefficients are only 0.07 in boreal summer (June–August) and −0.29 in boreal fall (SON) for the past 70 years (see section 2b). This suggests that it may not be ideal to rely only on the IOD to understand and monitor atmosphere–ocean processes over the tropical Indian Ocean and their climate impacts on the surrounding continents. It is, therefore, important to investigate SSTAs in the western and southeastern equatorial Indian Ocean individually and their driving mechanisms and impacts on regional climate.

The southeastern pole of the IOD has much greater variability than the western pole (Zhao and Hendon 2009) and is often characterized by the appearance of warm/cold SSTAs along the south and southwest coasts of Java and Sumatra, a phenomenon largely linked to wind-driven coastal upwelling (e.g., Susanto et al. 2001; Du et al. 2008) and thus referred to here as Java–Sumatra Niño/Niña (herein, JSN for the phenomenon in general and JS Niño/Niña for warm/cold events). Closely phase-locked to the seasonal cycle, JSN prevails largely in July–September (JAS), when the monsoonal winds are upwelling-favorable along the Java–Sumatra coast (i.e., southeasterly) and the coastal thermocline is relatively shallow (Susanto et al. 2001) (Figs. 1a,d). At times JSN appears as a precursor to the IOD, which becomes mature in October (Saji et al. 1999). In this study, JSN events are defined based on SSTAs averaged in the Java and Sumatra coastal regions (9° and 3°S, 95°–105°E and 12° and 6°S, 105°–115°E). See section 2a for more details.

Similar to the IOD, JSN events are linked to rainfall variability over the surrounding continents (Figs. 1c,f). For the IOD, these relationships are complex and often break down, partly due to the strong remote influence of El Niño–Southern Oscillation (ENSO) via changes in the Indo-Pacific Walker cells and extratropical stationary waves (e.g., Ashok et al. 2001, 2004; Cai et al. 2011; Lim et al. 2017; Ratna et al. 2020). Additionally, some IOD events are driven by ENSO (e.g., Shinoda et al. 2004; Behera et al. 2006; Hong et al. 2008b; Yang et al. 2015; Zhang et al. 2015; Stuecker et al. 2017), while others are driven by atmosphere–ocean processes internal to the Indian Ocean (e.g., Li et al. 2003; Fischer et al. 2005; Rao et al. 2009; Du et al. 2013;

Supplemental information related to this paper is available at the Journals Online website: https://doi.org/10.1175/JCLI-D-21-0616.s1.

Corresponding author: Sang-Ki Lee, sang-ki.lee@noaa.gov

DOI: 10.1175/JCLI-D-21-0616.1

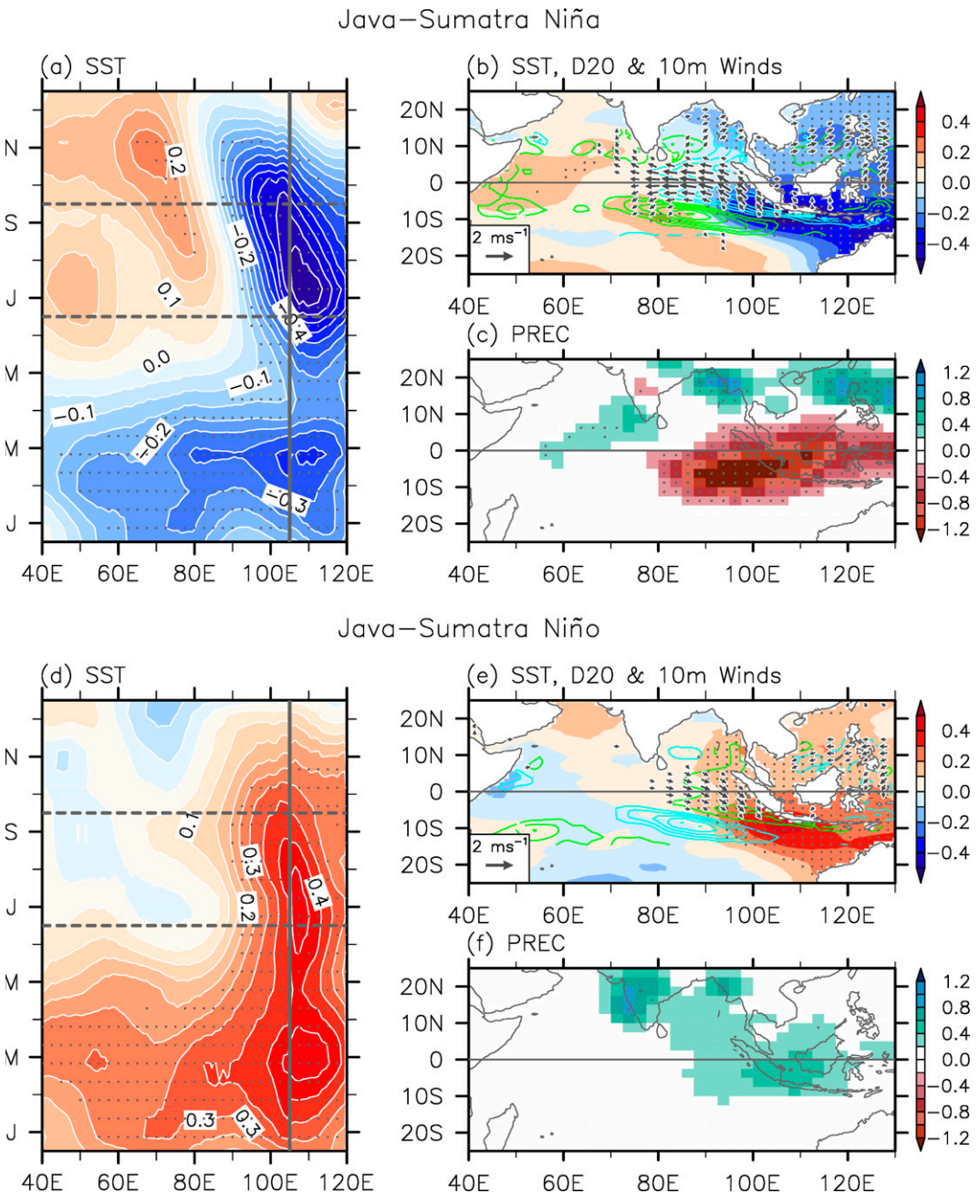

FIG. 1. (a),(d) Time–longitude plots of composite mean tropical south Indian SSTAs, averaged between 9° and 3°S along 40°–105°E and between 12° and 6°S along 105°–120°E, from January to December derived from observed JS Niña/Niño events. (b),(e) Composite mean tropical Indian Ocean SST (shading; °C), 20°C isotherm depth (D20; contours; m), and 10-m wind (vectors; m s^{-1}) anomalies; and (c),(f) precipitation anomalies (mm day^{-1}) during July–September derived from observed JS Niña/Niño events. Positive and negative D20 values are indicated by green and cyan contour lines, respectively. The dashed gray lines in (a) and (d) indicate 1 Jul and 30 Sep. The solid gray line in (a) and (d) indicates 105°E that separates the Java coastal region from the Sumatra coastal region. Wind vectors are shown only where wind speed anomalies are greater than 0.4 m s^{-1}. The contour interval for D20 anomalies is 2.5 m. Significant SSTA values at the 95% confidence level or above based on a Student's *t* test (two tailed) are indicated by gray dots in (a), (d), (b), and (e). Similarly, significant precipitation anomaly values at the 90% confidence level or above based on a Student's *t* test (two tailed) are indicated by gray dots in (c) and (f).

Sun et al. 2015; Yang et al. 2015; Stuecker et al. 2017; L.-Y. Zhang et al. 2020). These may also be applicable to JSN events. For instance, the 1997 JS Niña event occurred during the developing phase of the 1997/98 El Niño and contributed to the widespread Indonesian forest fires, which resulted in massive coral reef mortality events along the Java–Sumatra coast (Abram et al. 2003). In contrast, the 2019 JS Niña event, one of the strongest events ever recorded, developed rapidly in boreal summer under near-neutral ENSO conditions in the Pacific (Du et al. 2020; Wang et al. 2020), produced heavy rainfall and widespread severe flooding and landslides across South Asia (e.g., Srivastava et al. 2020), and caused extreme hot and dry conditions that contributed to severe forest fires over southeastern Australia (e.g., Lim et al. 2021; Tobin and Ganter 2020).

As briefly discussed, a significant gap still exists in our understanding of atmosphere–ocean variability in the tropical Indian Ocean. The main objectives of the present study are to describe and explain interannual variability of SST in the southeastern equatorial Indian Ocean associated with JSN and its impact on regional rainfall variability. To do so, we first present the basic characteristics of JSN. Next, to address large interevent variability of JSN, we present the spatiotemporal evolution patterns of the most frequently recurring JSN varieties and their links to ENSO and regional rainfall variability. We also present the potential onset mechanisms of the leading JSN varieties, followed by a discussion.

2. Data and methods

a. Data used

In this study, we analyze observational and reanalysis datasets to describe and explain JSN and its associated regional rainfall variability. Monthly SSTAs are derived from the Centennial In Situ Observation-Based Estimates of the variability of SST (Ishii et al. 2005) for the 1949–2019 period. Monthly anomalies of surface winds (at 10 m) and 850-hPa winds are from the National Centers for Environmental Prediction–National Center for Atmospheric Research reanalysis (Kalnay et al. 1996) for the same period. Monthly precipitation anomalies are derived from the National Oceanic and Atmospheric Administration's precipitation reconstruction dataset (Chen et al. 2002) for the same period. Monthly anomalies of 20°C isotherm depth (D20), which are used here as proxies for thermocline depth anomalies, are obtained from European Centre for Medium-Range Weather Forecasts Ocean Reanalysis System 5 (Zuo et al. 2017) for the 1958–2018 period.

b. Identification of JSN and ENSO events

SSTAs in the tropical Indian Ocean are influenced by strong warming trends and decadal variability (Han et al. 2014; Lim et al. 2017). For instance, without detrending, the correlation between the western and southeastern poles of the IOD in SON is 0.23 during 1949–2019, 0.00 during 1949–80, and −0.25 during 1981–2019. Since we are mainly interested in interannual variability, a separate 30-yr averaged climatology is constructed every 5 years and used to derive SSTAs. For instance, to compute SSTAs for the 1951–55 period, a 30-yr averaged climatology for 1936–65 is used; to compute SSTAs for 1956–60, a 30-yr averaged climatology for 1941–70 is used; and so forth. This method defines JSN events relative to their contemporary climatology. It is also currently being used at the National Oceanic and Atmospheric Administration's Climate Prediction Center to define El Niño and La Niña events. One way to define JSN Niño/Niña events is based on the threshold that the 3-month averaged SSTAs exceed ±0.4°C in the Java–Sumatra coastal region (9° and 3°S, 95°–105°E and 12° and 6°S, 105°–115°E) for at least three consecutive overlapping seasons. An alternative method is to apply the same threshold separately for the south coast of Java (12°–6°S and 105°–115°E) and the southwest coast of Sumatra (9°–3°S and 95°–105°E), and then identify JSN events when the threshold is met in either of the two regions. We identify 17 JS Niña and 14 JS Niño events based on the first method, and 21 JS Niña and 19 JS Niño events based on the second method (supplementary Tables 1–4). The second method is used in this study because of the larger sample size. We also use 26 El Niño and 25 La Niña events identified based on a threshold that the 3-month averaged SSTA in Niño-3.4 region (120°–170°W and 5°S–5°N) is equal to or exceeds ±0.5°C for at least five consecutive months (Lee et al. 2014, 2018) (supplementary Table 4).

c. Spatiotemporal EOF analysis

A longitude–time map of tropical south Indian SSTAs is derived for each of the 21 JS Niña and 19 JS Niño events (supplementary Figs. 1 and 2). The time and longitude axes span from January to December and the entire Indian Ocean (40°–120°E), respectively. Note that tropical south Indian SSTAs are averaged between 9° and 3°S west of 105°E, and between 12° and 6°S east of 105°E in order to take into account the difference in latitude bands between the Java coast and Sumatra coast. To objectively identify the preferred spatiotemporal modes of the observed JS Niña events, we perform an empirical orthogonal function (EOF) analysis of the 21 longitude–time maps of tropical south Indian SSTAs, following the method used in Lee et al. (2014). The resulting principal components (PCs) are associated with each individual JS Niña event, and the EOFs represent a linearly independent set of longitude–time maps. The first and second leading PCs explain 36% and 13% of the interevent variance, respectively (supplementary Figs. 3b,c). The same EOF analysis is performed to identify the preferred spatiotemporal modes of the 19 observed JS Niño events for which the first and second leading PCs explain 27% and 23% of the interevent variance, respectively (supplementary Figs. 3e,f). Note that the same method was previously used to identify the leading spatiotemporal modes of the observed El Niño events in the Pacific (Lee et al. 2014, 2018) and Atlantic Niño events in the Atlantic (Vallès-Casanova et al. 2020).

While the first two EOFs for JS Niña are well separated, the first two EOFs for JS Niño are not, and thus do not pass the North test (North et al. 1982), which is based on an estimate of the sampling errors of each eigenvalue. For the

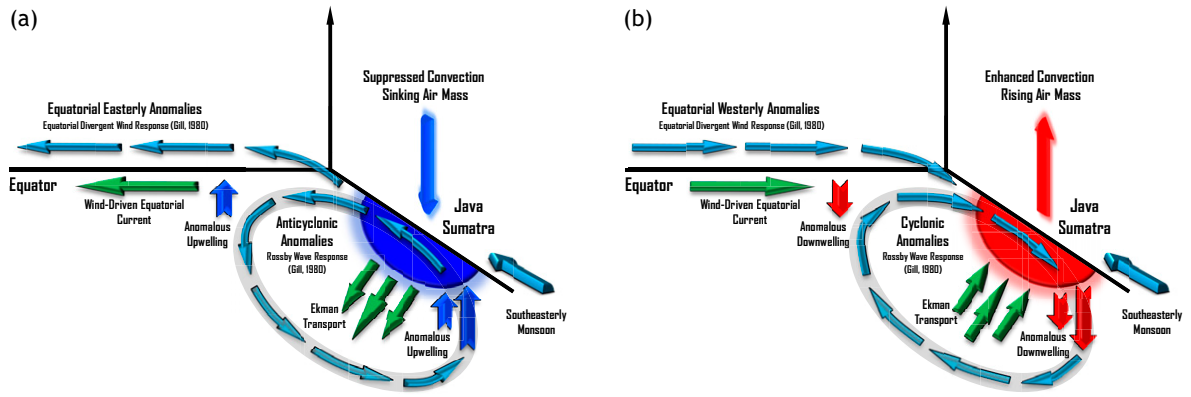

FIG. 2. The schematics illustrate local Bjerknes feedback mechanisms for (a) JS Niña and (b) JS Niño in austral winter and spring (under the southeasterly monsoon). (a) The cold SSTAs off the Java–Sumatra coast suppress atmospheric convection aloft. The associated heat sink induces an anomalous anticyclone to its west (i.e., a Rossby wave response), producing southeasterly wind anomalies and anomalous upwelling off the Java–Sumatra coast, which in turn reinforce the initial cooling. The equatorial easterly wind anomalies driven by the heat sink (i.e., an equatorial divergent wind response) produce anomalous upwelling in the eastern equatorial Indian Ocean, promoting an expansion of the cold SSTAs toward the equator along the Sumatra coast. (b) The local Bjerknes feedback mechanism for JS Niño can be explained by the opposite patterns of anomalies for JS Niña. These schematics are adopted and revised from Li et al. (2003).

majority of JS Niño events, however, their PC values align reasonably well with either PC1 or PC2 axis, whereas the 1961 JS Niño event is a mixture of the two EOFs and is therefore an outlier (Fig. 3j). Indeed, replacing the 1961 JS Niño event with the 2001 warm event, which exceeds the threshold for two consecutive overlapping seasons (see Table S1 and S2), the two leading EOFs are well separated (PC1 = 28%, and PC2 = 19%) and pass the North test. Nevertheless, the 1961 JS Niño event is retained in this study because it still meets the criteria, and the PC values for the majority of JS Niño events align well with either PC1 or PC2 axis.

3. Results

a. *Basic characteristics of JSN*

As shown in Fig. 1a, JS Niña often develops as early as April–June (AMJ) along the south coast of Java, peaks in JAS as the cold SSTAs slowly shift to the southwest coast of Sumatra, and dissipates in October–December (OND). Although weak, there is a secondary peak of JS Niña in the preceding January–March (JFM; herein, preseason). This preseason cooling pattern is closely tied to a basinwide cooling of the tropical Indian Ocean that is largely modulated by the Indian Ocean basin (IOB) mode, which tends to occur during the dissipation phase of La Niña in boreal winter and spring (Yang et al. 2007), as discussed later in this study. Interestingly, relatively weak warm SSTAs develop in the central tropical south Indian Ocean in JAS, and then propagate westward to produce a positive IOD-like pattern in OND.

During the most active months (JAS), JS Niña is typically characterized by cold SSTAs, a shallower thermocline, southeasterly surface wind anomalies along the Java–Sumatra coast, a deeper thermocline farther westward in the tropical south Indian Ocean, and easterly surface wind anomalies along the eastern equatorial Indian Ocean (Fig. 1b). These anomalous atmosphere–ocean patterns indicate that local Bjerknes feedback plays an important role in the development of JS Niña in austral winter and spring (e.g., Li et al. 2003). More specifically, the cold SSTAs off the Java–Sumatra coast suppress atmospheric convection aloft. The associated heat sink induces an anomalous anticyclone to its west (i.e., a descending Rossby wave response; Gill 1980), producing southeasterly wind anomalies and anomalous upwelling off the Java–Sumatra coast, which in turn reinforce the initial cooling (Li et al. 2003). The heat sink also drives equatorial easterly wind anomalies (i.e., an equatorial divergent wind response; Gill 1980), thus producing anomalous upwelling in the eastern equatorial Indian Ocean and promoting an expansion of the cold SSTAs toward the equator along the Sumatra coast (Fig. 2a).

JS Niño is characterized by nearly opposite patterns of anomalous SSTs, thermocline depth and surface winds compared to JS Niña (Figs. 1d,e), and thus subject to local Bjerknes feedback for its development in austral winter and spring (Fig. 2b). However, there are several noticeable differences that break the antisymmetry. In particular, JS Niño tends to develop and decay slightly earlier than JS Niña in boreal summer and fall, and the associated atmosphere–ocean anomalies are generally much weaker (e.g., Hong et al. 2008a; Cai and Qiu 2013). In contrast, the preseason peak in JFM, which is tied to a positive phase of the IOB mode and the dissipation phase of El Niño (Yang et al. 2007), has a much larger amplitude, being on par with the peak amplitude in June–August. Additionally, unlike JS Niña, JS Niño tends to remain a monopole throughout boreal summer and fall.

JS Niña events are linked to decreased rainfall over the Maritime Continent (i.e., maritime Southeast Asia) and the Malay Peninsula, and vice versa for JS Niño events (Figs. 1c,f). Some JS Niña/Niño events are also linked to increased rainfall

in South Asia and mainland Southeast Asia (herein, South–Southeast Asia). However, these and other basic characteristics of JSN derived from the composite mean fields (Fig. 1) are not applicable to all events. Indeed, the spatiotemporal evolution patterns are quite different between individual events in terms of the timing, zonal pattern, and amplitude of their onset, peak, and dissipation (supplementary Figs. 1 and 2).

b. Spatiotemporal diversity of JSN

As described in section 2c, we carry out a spatiotemporal EOF analysis to identify the first two preferred modes of the observed JS Niño/Niña events. Each EOF mode for warm/cold events represents two contrasting JS Niño/Niña varieties or flavors (PC changing from −1 to 1) that correspond to adding and subtracting the EOF pattern to the composite mean, leading to four sets of the most frequently recurring JS Niño/Niña varieties. See section 2c and supplementary Fig. 3 for more details.

One of the leading JS Niño/Niña varieties describes warm/cold events that form in JAS and thus is referred to as *the on-season JS Niño/Niña variety* (Figs. 3f,h). The 1989 warm event and the 1994 cold event are good examples of the on-season JS Niño/Niña variety (Figs. 3i,j; see also supplementary Figs. 1 and 2). Other JS Niño/Niña varieties describe warm/cold events that appear as early as JFM and then, after a short pause, reappear in JAS (herein, *the double-peak JS Niño/Niña variety*; Figs. 3e,g) or almost completely dissipate before boreal summer (herein, *the preseason JS Niño/Niña variety*; Figs. 3a,c). The 2016 warm event is an example of the former, while the 1974 cold event and the 1983 warm event are examples of the latter (see also supplementary Figs. 1 and 2). Note, however, that these JS Niña and Niño varieties are not exactly in mirror-image patterns. In particular, SSTAs along the Java–Sumatra coast associated with the double-peak JS Niño variety are much stronger than those associated with the double-peak JS Niña variety. On the other hand, the SSTAs associated with the on-season JS Niño variety are weaker than those associated with the on-season JS Niña variety.

Occasionally, strong cold events may develop in boreal summer, persist throughout SON and spawn robust warm SSTAs in the central tropical south Indian Ocean, which in turn propagate westward and peak in OND. The spatiotemporal evolution of such strong and persistent cold events (e.g., the 2019 JS Niña) is well captured by *the persistent JS Niña variety* (Fig. 3b). Finally, although rare and very weak in amplitude, a preseason warm event may switch to a cold event in the boreal summer (herein, *the transition JS Niño variety*; Fig. 3d).

It is worth noting that the persistent JS Niña variety, which shows the greatest cooling along the Java–Sumatra coast, displays a positive IOD-like pattern in OND, whereas the double-peak JS Niño variety, which shows the greatest warming along the Java–Sumatra coast, prevails largely as a monopole throughout boreal summer and fall. Both the double-peak JS Niña and on-season JS Niño varieties display an IOD-like pattern in boreal summer, while the on-season JS Niña variety has a more complex zonal tripole structure similar to IOD Modoki and Indian Ocean tripole mode discussed in previous studies (Endo and Tozuka 2016; Y. Zhang et al. 2020).

c. Interactions with ENSO

The preseason and double-peak JS Niño/Niña varieties are strongly connected to the dissipating phase of El Niño/La Niña and the associated IOB mode in boreal spring (Figs. 4a,c,e,g). Specifically, the preseason JS Niño/Niña variety is favored if El Niño/La Niña dissipates into an ENSO-neutral phase in boreal summer, whereas the double-peak JS Niño/Niña variety is favored if El Niño/La Niña transitions to the opposite phase and then intensifies during boreal summer and fall. However, some double-peak JS Niño/Niña events occurred under a near-neutral ENSO condition in JAS (e.g., the 2016 JS Niño; supplementary Figs. 4 and 5). In contrast, there is no apparent ENSO signal linked to the on-season JS Niño/Niña variety in boreal summer and fall. This suggests that the on-season JS Niño/Niña variety is predominantly driven by atmosphere–ocean processes internal to the Indian Ocean. Similarly, the transition JS Niño variety seems to have little connection to ENSO.

Perhaps the most interesting case is the persistent JS Niña variety, which is characterized by the greatest intensity of cold SSTAs off the Java–Sumatra coast. During these events, strong warm SSTAs develop in the southwestern equatorial Indian Ocean around OND, so this variety can also be described as strong positive IOD. The persistent JS Niña variety is associated with the developing phase of El Niño, but the regressed ENSO signal is relatively weak, especially during the onset phase of the persistent JS Niña variety around May–July (Fig. 4b). Therefore, it is unlikely that ENSO is required for the onset of the persistent JS Niña variety. Instead, it is likely driven by atmosphere–ocean processes internal to the Indian Ocean.

To further study the potential role of ENSO in driving the JSN varieties, longitude–time composite maps of SSTAs along the equatorial Pacific and tropical south Indian Oceans are constructed for observed El Niño and La Niña events during 1949–2019 (Figs. 4i,j). There is an overall weak connection between the developing phase of ENSO and SSTAs along the Java–Sumatra coast. An IOD-like pattern of SSTAs emerges around SON from the southeastern equatorial Indian Ocean to the western equatorial Indian Ocean. However, during the onset phase of JSN (i.e., prior to July), equatorial Pacific SSTAs associated with the developing phase of ENSO are relatively weak; thus, it is unlikely that ENSO drives the onset of JSN. The remote influence of ENSO during the onset, peak and dissipation phases of JSN, and the associated regional rainfall patterns, are further investigated next.

d. Regional rainfall patterns linked to JSN varieties

To describe the atmosphere–ocean processes associated with different JSN varieties, the corresponding spatiotemporal patterns of oceanic and atmospheric variables (i.e., precipitation, surface winds, SST, and D20) are obtained by linearly regressing their time series onto the first and second leading

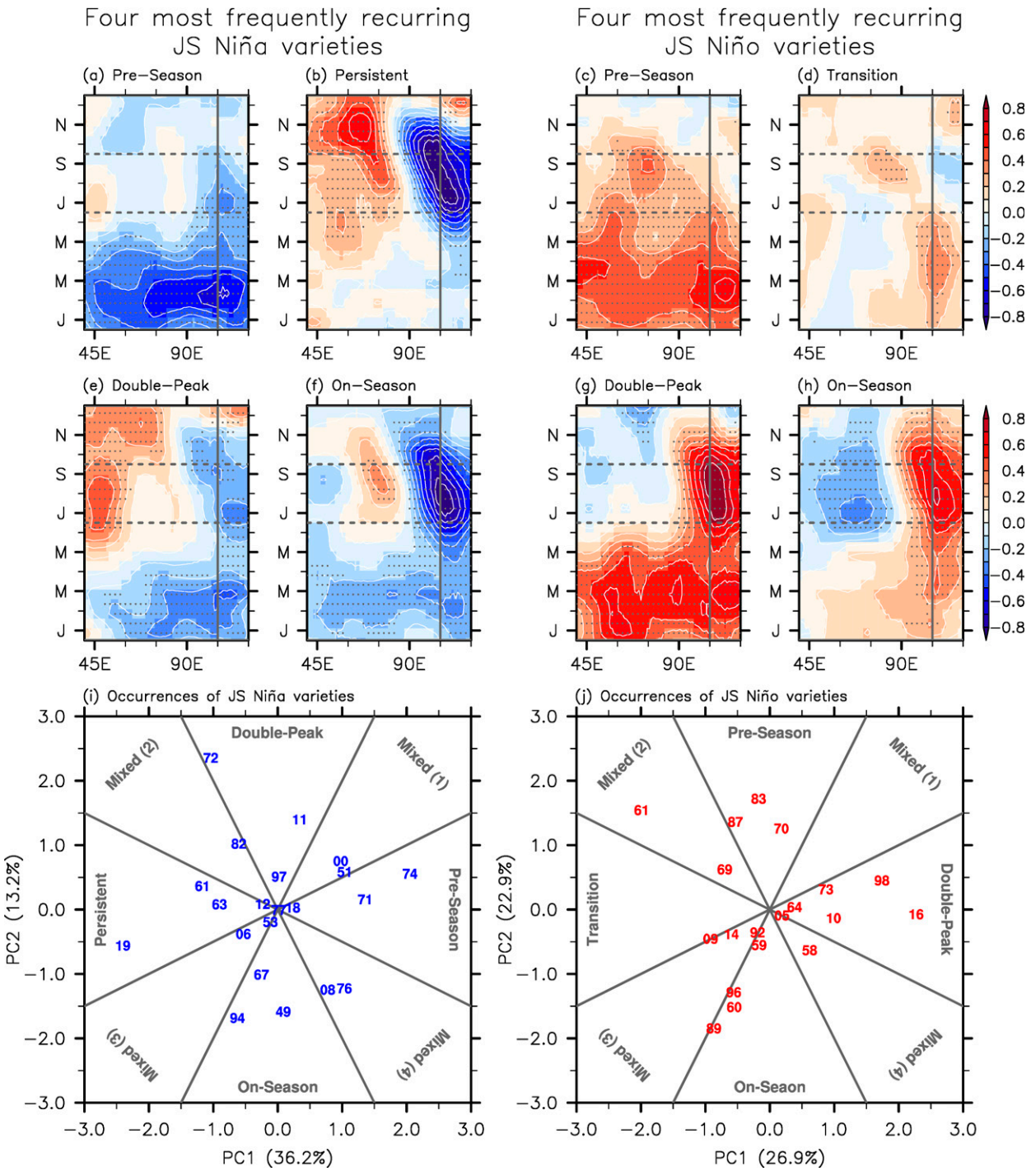

FIG. 3. Time–longitude plots of the tropical south Indian SSTAs (°C; averaged over 9°–3°S for 40°–105°E and over 12°–6°S for 105°–120°E; shades) illustrating the four most frequently recurring JS Niña varieties, namely, (a) the preseason, (b) persistent, (e) double-peak, and (f) on-season, and the four most frequently recurring JS Niño varieties, namely, (c) the preseason, (d) transition, (g) double-peak, and (h) on-season during 1949–2019. Significant SSTA values at the 95% confidence level or above based on a Student's *t* test (two tailed) are indicated by gray dots in (a)–(h). (i),(j) Normalized PC1 vs PC2 values for the 21 JS Niña and 19 JS Niño events. The two-digit numbers in blue indicate the JS Niña years, while those in red indicate the JS Niño years. The percentage values shown in (i) and (j) indicate the interevent variances explained by the PCs. The dashed gray lines in (a)–(h) indicate 1 Jul and 30 Sep. The solid gray line in (a)–(h) indicates 105°E that separates the Java coastal region from the Sumatra coastal region. The thick gray lines in (i) and (j) are the boundaries (i.e., PC1 = ±2 × PC2 and PC2 = ±2 × PC1) that separate the four sets of varieties from the mixed varieties.

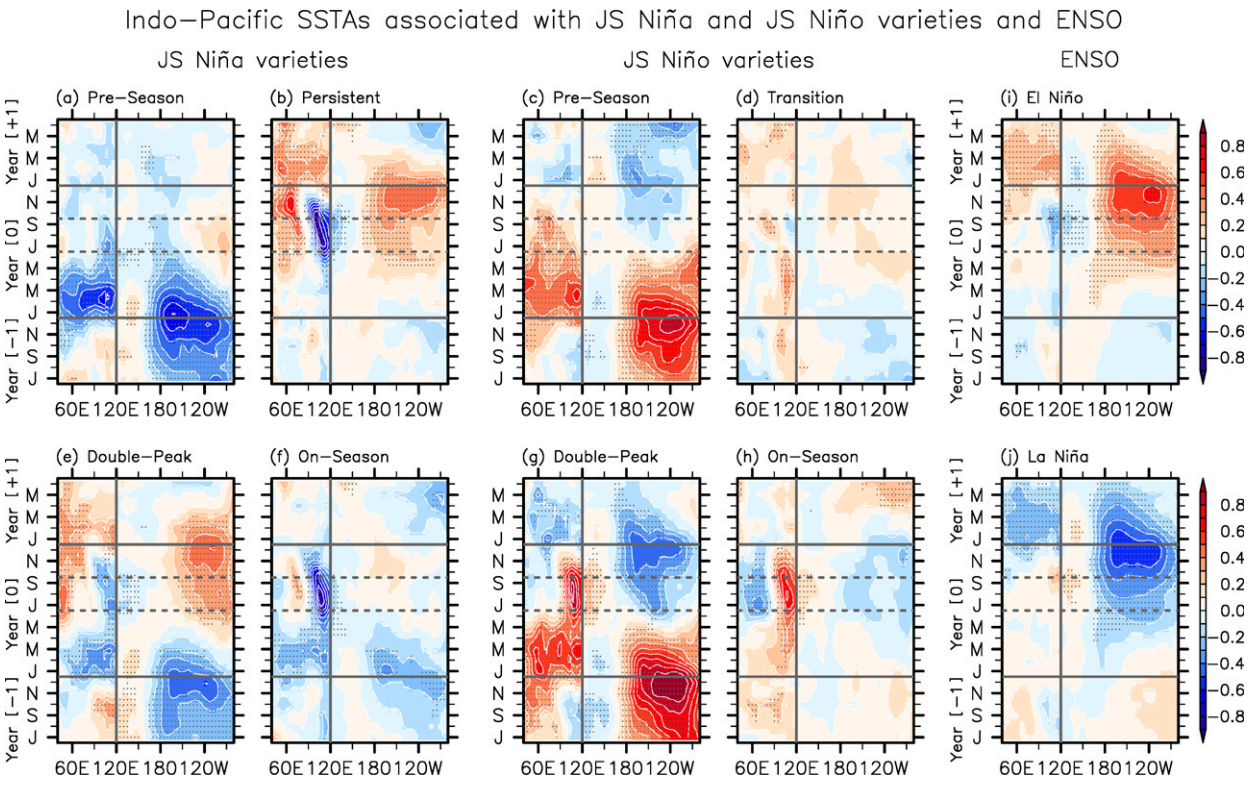

FIG. 4. Time–longitude plots of SSTAs (°C) along the equatorial Pacific (averaged over 5°S–5°N) and tropical south Indian Oceans (averaged over 9°–3°S along 40°–105°E and over 12°–6°S along 105°–120°E) for (a),(b),(e),(f) the four most frequently recurring JS Niña varieties and for (c),(d),(g),(h) the four most frequently recurring JS Niño varieties, and for (i),(j) ENSO, spanning from July (−1) to June (+1). The time–longitude plots for ENSO are based on composite mean SSTAs derived from observed El Niño and La Niña events. The horizontal dashed gray lines indicate 1 Jul (0) and 30 Sep (0), while the horizontal solid gray lines indicate 1 Jan (0) and 31 Dec (0). The vertical solid gray line indicates 120°E that separates the Indian Ocean from the Pacific Ocean. SSTAs in the tropical Pacific Ocean have been multiplied by 0.5 for better visual comparison with SSTAs in the tropical Indian Ocean. Significant SSTA values at the 95% confidence level or above based on a Student's *t* test (two tailed) are indicated by gray dots.

PCs of the observed JS Niño/Nina events. For instance, we first subsample 21 maps of precipitation anomalies averaged in any season (e.g., AMJ) for the 21 years during which JS Niña occurred. Then, they are regressed on to the 21 values of PC2 for the JS Niña events. The regression coefficients are then added to the composite mean of the 21 maps of precipitation anomalies to obtain the anomalous rainfall patterns for the double peak JS Niña variety. Similarly, the regression coefficients are subtracted from the composite mean to obtain the anomalous rainfall patterns for the on-season JS Niña variety. The same method is used to obtain anomalous rainfall patterns for the preseason and persistent JS Niña varieties from PC1 and for the anomalous rainfall patterns for the JS Niño varieties.

Figure 5 shows the rainfall and 850-hPa wind anomalies associated with El Niño and the leading JS Niña varieties for the onset (AMJ), peak (JAS), and dissipation (OND) phases of JS Niña. During the onset phase of JS Niña, rainfall anomalies associated with JS Niña varieties are generally small because the corresponding SSTAs in the southeastern equatorial Indian Ocean are normally very weak. During the peak phase of JS Niña, the rainfall anomalies associated with El Niño show a predominantly zonal seesaw pattern with decreased rainfall over the Maritime Continent extending to India (e.g., Kumar et al. 2006) and increased rainfall in the western tropical Pacific (Fig. 5b). The anomalous low-level westerly winds along the western tropical Pacific clearly indicate a weakened Pacific Walker cell. The rainfall and low-level wind anomalies during the peak phase of the double-peak JS Niña variety are largely consistent with those of El Niño (Fig. 5e), suggesting that the remote influence of El Niño via changes in the Pacific Walker cell largely dictates the regional rainfall anomalies associated with the double-peak JS Niña variety.

In contrast, the rainfall anomalies during the peak phase of the persistent JS Niña variety show a meridional seesaw pattern between the Maritime Continent and South–Southeast Asia (Fig. 5h). The associated anomalous low-level winds suggest a Gill-type cross-hemispheric atmospheric response to diabatic cooling anomalies aloft in the southeastern equatorial Indian Ocean (Gill 1980). The Gill-type atmospheric circulation carries extra moisture from the southeastern equatorial Indian Ocean region to South–Southeast Asia, enhancing monsoonal rainfall in countries and regions surrounding the

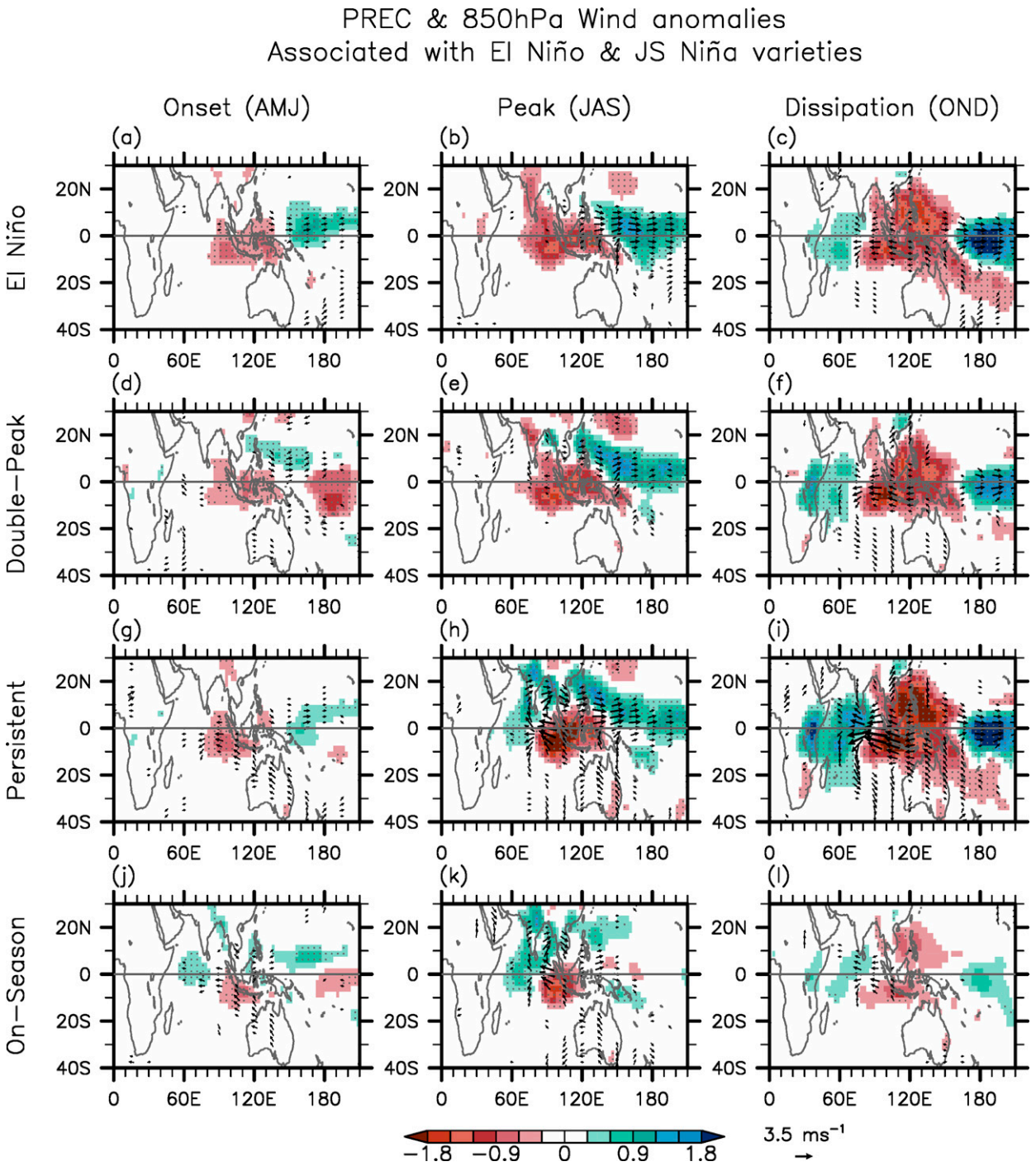

FIG. 5. Precipitation (shaded; mm day^{-1}) and 850-hPa wind anomalies (vectors; m s^{-1}) associated with (a)–(c) El Niño and (d)–(f) the double-peak, (g)–(i) persistent, and (j)–(l) on-season JS Niña varieties during the onset, peak, and dissipation phases of JS Niña. For El Niño composite mean variables are shown, while for the JS Niña varieties regression variables are shown. See section 3d for more details. Significant precipitation anomaly values at the 90% confidence level or above based on a Student's *t* test (two tailed) are indicated by gray dots. Wind vectors are shown only where wind speed anomalies are greater than 0.6 m s^{-1}.

Bay of Bengal and the South China Sea (e.g., India, Bangladesh, Myanmar, Thailand, Vietnam, and South China), and thus can be interpreted as a strengthening of the South and Southeast Asian summer monsoons. The on-season JS Niña variety during its peak phase shows a similar meridional seesaw pattern of rainfall anomalies and the Gill-type atmospheric response, though the rainfall and low-level wind anomalies are generally weaker than those of the persistent

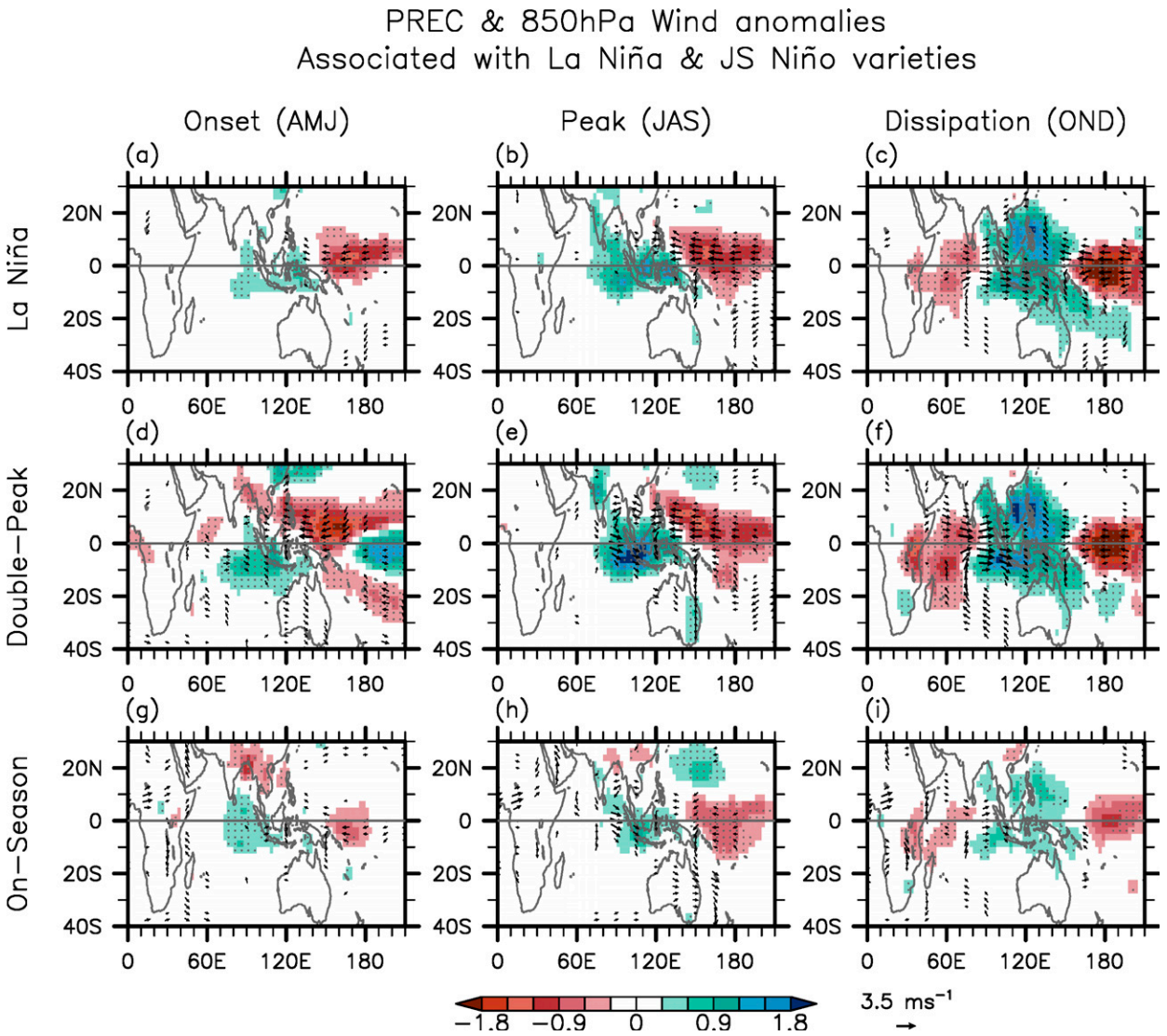

FIG. 6. Precipitation (shaded; mm day^{-1}) and 850 hPa wind anomalies (vectors; m s^{-1}) associated with (a)–(c) La Niña and (d)–(f) the double-peak and (g)–(i) on-season JS Niño varieties during the onset, peak, and dissipation phases of JS Niño. For La Niña composite mean variables are shown, while for the JS Niño varieties regression variables are shown. Significant precipitation anomaly values at the 90% confidence level or above based on a Student's t test (two tailed) are indicated by gray dots. Wind vectors are shown only where wind speed anomalies are greater than 0.6 m s^{-1}.

JS Niña variety (Fig. 5k). Additionally, the teleconnection to southeastern Australia, which is known to occur in boreal summer during some IOD events (Cai et al. 2011), is observed only during the peak phase of the persistent JS Niña variety (Fig. 5h).

During the dissipation phase (OND) of JS Niña, the rainfall anomalies associated with El Niño and the double-peak, persistent and on-season JS Niña varieties all show a zonal tripole pattern with increased rainfall from eastern Africa to the western tropical Indian Ocean, decreased rainfall over and around the Maritime Continent, and increased rainfall over the western tropical Pacific Ocean (Figs. 5c,f,i,l). The zonal tripole pattern of rainfall anomalies that appears during the dissipation phase of the persistent JS Niña variety is particularly strong, with large rainfall anomalies over eastern Africa, northern Australia, and the Maritime Continent, whereas the rainfall response to the on-season JS Niña variety is generally very weak in OND.

Figure 6 shows the rainfall and 850-hPa wind anomalies associated with La Niña and the leading JS Niño varieties for the onset, peak and dissipation phases of JS Niño. The rainfall and low-level wind anomalies associated with La Niña are almost mirror images of those associated with El Niño, indicating a zonal seesaw pattern of rainfall anomalies and a strengthened Pacific Walker cell during the peak phase of JS Niño (Fig. 6b). During the onset phase of JS Niño, rainfall

anomalies associated with the on-season JS Niño variety are very small because the corresponding SSTAs in the southeastern equatorial Indian Ocean are very weak. The rainfall anomalies associated with the double-peak JS Niña variety are larger and appear to be associated with El Niño, which drives the preseason warming of the equatorial Indian Ocean, rather than forced by the preseason warm SSTAs themselves.

During the peak phase of JS Niño, the rainfall and low-level wind anomalies associated with the double-peak JS Niño variety are largely consistent with those of La Niña (Fig. 6e). Interestingly, Gill-type atmospheric circulation anomalies still appear during the peak phase in response to diabatic heating anomalies over the southeastern equatorial Indian Ocean. However, these anomalies are not robust enough to produce a meridional seesaw pattern of rainfall anomalies between the Maritime Continent and South–Southeast Asia. Similarly, the anomalous low-level winds associated with the peak phase of the on-season JS Niño variety show a Gill-type atmospheric response to diabatic heating anomalies over the southeastern equatorial Indian Ocean (Fig. 6e). The associated regional rainfall anomalies are somewhat indicative of a meridional seesaw pattern. However, the rainfall response to the on-season JS Niño variety is generally weak.

During the dissipation phase (OND) of JS Niño, the rainfall anomalies associated with La Niña and the double-peak and on-season JS Niño varieties are characterized by a zonal tripole pattern with decreased rainfall from eastern Africa to the western tropical Indian Ocean, increased rainfall over the Maritime Continent and over northern and eastern Australia, and decreased rainfall over the western tropical Pacific Ocean (Figs. 6c,f,i). However, the rainfall response to the on-season JS Niño variety is very weak in OND.

e. Onset mechanisms of JSN varieties

As discussed earlier, the preseason and double-peak JS Niño/Niña and persistent JS Niña varieties are connected to ENSO, while the on-season JS Niño/Niña variety is largely independent of ENSO. Here, we explore in more detail the onset mechanisms of leading JSN varieties. First, we examine the anomalous SSTs, thermocline depth and surface winds associated with El Niño/La Niña and then compare them with those of the leading JS Niña/Niño varieties during the onset, peak and dissipation phases of JSN (Figs. 7 and 8).

SSTAs in the tropical Indian Ocean associated with El Niño are generally weak (Figs. 7a–c). Although weak cold SSTAs appear in a broad region of the southeastern tropical Indian Ocean during the peak phase (JAS) of JS Niña, the surface wind anomalies are too weak to trigger or sustain JS Niña. A positive IOD-like pattern of weak SSTAs develops during the dissipation phase (OND) of JS Niña, with corresponding surface wind anomalies (i.e., southeasterly) that are favorable for coastal upwelling along the Java–Sumatra coast and downwelling in the central tropical south Indian Ocean. However, since the southeasterly monsoonal wind weakens and can reverse its direction as the Australian summer monsoon develops (e.g., Hendon et al. 2012), the seasonal mean atmosphere–ocean conditions along the Java–Sumatra coast become unfavorable for local Bjerknes feedback in OND (supplementary Fig. 6). For the double-peak JS Niña variety, cold SSTAs appear in the southeastern tropical Indian Ocean during its onset phase (AMJ), with almost no surface wind anomalies in the region (Fig. 7d). This suggests that the cold SSTAs are the residual of basinwide cold SSTAs forced remotely during the dissipating phase of La Niña (Fig. 4e). Although still weak, the anomalous SSTs, thermocline depth and surface winds during the peak and dissipation phases of JS Niña are generally larger than those of El Niño (Figs. 7e,f), suggesting an involvement of local Bjerknes feedback in the double-peak JS Niña variety, possibly enhanced by the residual of cold SSTAs formed during the preseason.

Unlike El Niño or the double-peak JS Niña variety, a robust pattern of upwelling favorable surface wind anomalies appears along the central and southeastern equatorial Indian Ocean during the onset phase of the persistent JS Niña variety (Fig. 7g). Although weak, cold SSTAs appear along the south coast of Java, and the thermocline becomes shallower from the south coast of Java to the northeast equatorial region off Sumatra. During the peak phase, the anomalous surface winds strengthen greatly, and the cold SSTAs intensify and expand to the southwest coast of Sumatra (Fig. 7h). Additionally, the thermocline becomes shallower along the Java–Sumatra coast and in the eastern equatorial region, and the anomaly expands to the west. In contrast, warm SSTAs and a deeper thermocline develop in the central tropical south Indian Ocean. These patterns of amplifying surface wind, SST, and thermocline depth anomalies from the onset to peak phase strongly suggest an active role of local Bjerknes feedback.

During the dissipation phase of the persistent JS Niña variety, the cold SSTAs off the Java–Sumatra coast persist but weaken, while the anomalous patterns of surface winds and thermocline depth further intensify and propagate westward (Fig. 7i). These surface wind and thermocline depth anomalies are accompanied by a pronounced basinwide seesaw pattern of SSTAs between the southeast and southwestern tropical Indian Ocean, thus producing a strong positive IOD. Although the surface wind anomalies are still strong and upwelling favorable, the cold SSTs along the Java–Sumatra coast start to weaken in OND as the southeasterly monsoonal wind weakens and the seasonal mean thermocline along the Java–Sumatra coast becomes too deep to influence the coastal SSTs. This also explains how the weakening and directional shifts in monsoonal winds in boreal winter prevent JSN from continuing beyond OND (supplementary Fig. 6).

The spatial patterns and amplitudes of anomalous SSTs, thermocline depth and surface winds associated with the on-season JS Niña variety are very similar to those of the persistent JS Niña variety during the onset and peak phases (Figs. 7j,k). However, unlike the persistent JS Niña variety, the anomalous SSTs and surface winds diminish rapidly in OND (Fig. 7l). It is not entirely clear why some JS Niña events are persistent (i.e., the persistent JS Niña variety) and others dissipate more quickly (i.e., the on-season JS Niña variety). One possibility is that some JS Niña events are enhanced and prolonged by remote forcing from the Pacific. Another possibility

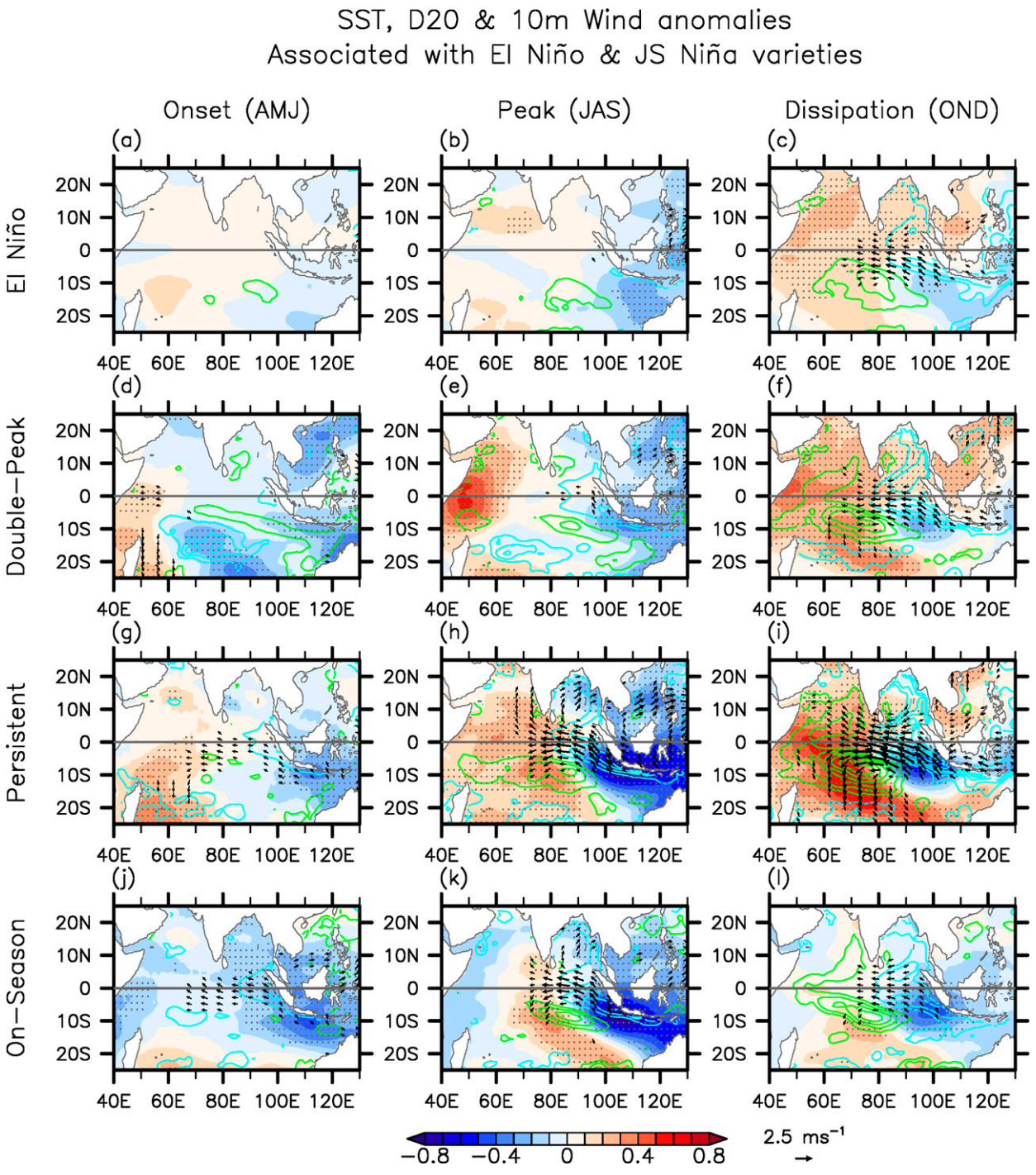

FIG. 7. SST (shaded; °C), D20 (contours; m), and 10 m wind (vectors; m s^{-1}) anomalies associated with (a)–(c) El Niño and (d)–(f) the double-peak, (g)–(i) persistent, and (j)–(l) on-season JS Niña varieties during the onset, peak, and dissipation phases of JS Niña. Positive and negative D20 values are indicated by green and cyan contour lines, respectively. For El Niño, composite mean variables are shown; for the JS Niña varieties, regression variables are shown. Significant SSTA values at the 95% confidence level or above based on a Student's *t* test (two tailed) are indicated by gray dots. Wind vectors are shown only when wind speed anomalies are greater than 0.6 m s^{-1}. The contour interval for D20 anomalies is 5 m.

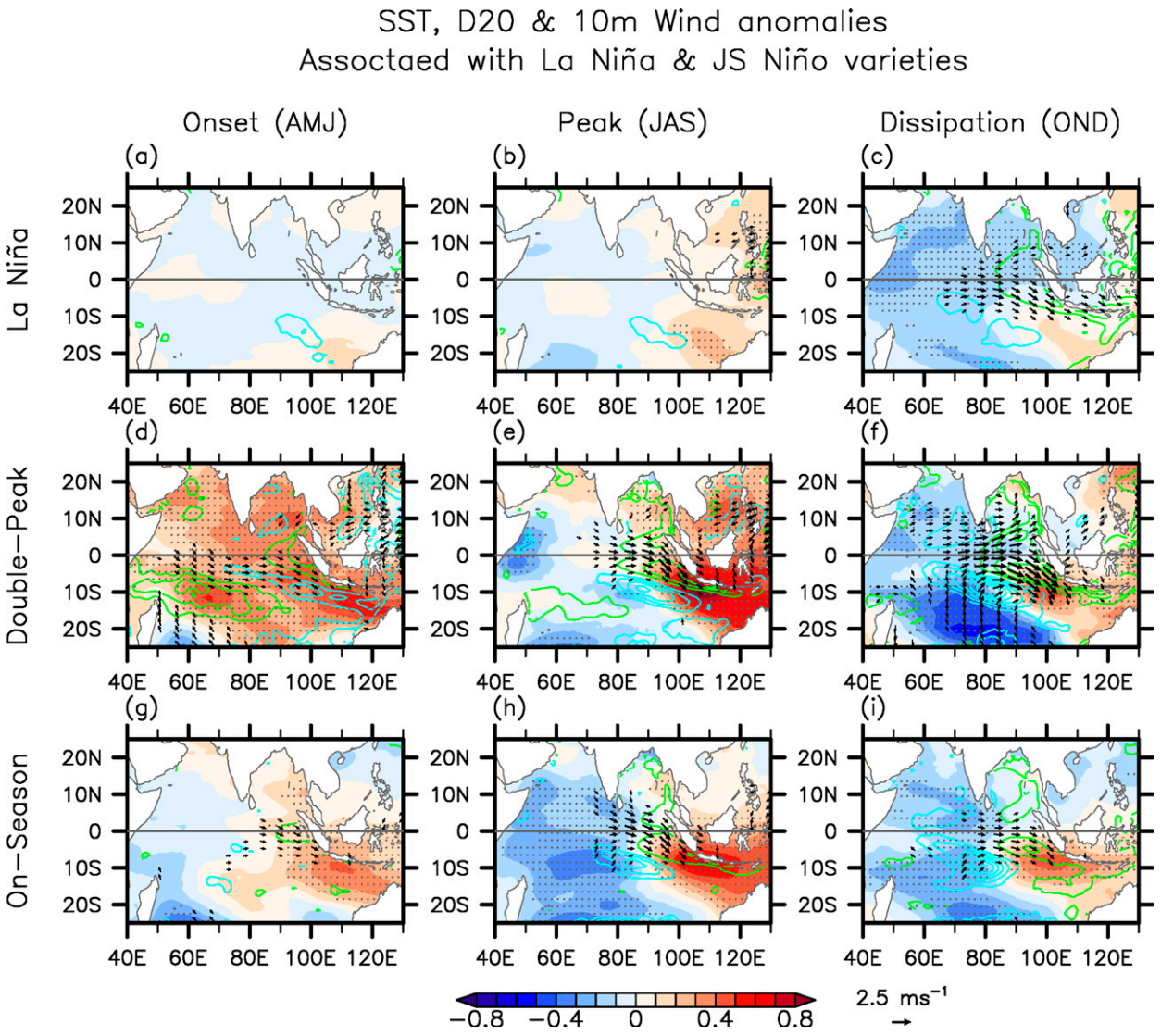

FIG. 8. SST (shaded; °C), D20 (contours; m), and 10 m wind (vectors; m s^{-1}) anomalies associated with (a)–(c) La Niña and (d)–(f) the double-peak and (g)–(i) on-season JS Niño varieties during the onset, peak, and dissipation phases of JS Niño. Positive and negative D20 values are indicated by green and cyan contour lines, respectively. For La Niña composite mean variables are shown, while for the JS Niño varieties regression variables are shown. Significant SSTA values at the 95% confidence level or above based on a Student's *t* test (two tailed) are indicated by gray dots. Wind vectors are shown only where wind speed anomalies are greater than 0.6 m s^{-1}. The contour interval for D20 anomalies is 5 m.

is that an exceptionally strong JS Niña event may greatly weaken the Indo-Pacific Walker cells, producing warm SSTAs in the neighboring regions of the tropical Indian and Pacific Oceans. The warm SSTAs in the tropical Indian and Pacific Oceans may in turn further weaken the Indo-Pacific Walker cells to prolong the JS Niña event in OND. Consistent with this hypothesis, the persistent JS Niña variety is linked to warm SSTAs in the southwestern tropical Indian Ocean and weak El Niño conditions (Fig. 4b), but there are almost no such warm SSTAs for the on-season JS Niña variety (Fig. 4f). This hypothesis is also in line with the idea that a strong IOD event may induce a weak (or pseudo) ENSO event (Izumo et al. 2010; Lim and Hendon 2017; Luo et al. 2010; Wu and Kirtman 2004).

Anomalous SSTs, surface winds and thermocline depth associated with La Niña are more or less mirror images of those associated with El Niño (Figs. 8a–c). In other words, the anomalies are too weak to trigger or sustain JS Niño during the onset (AMJ) and peak (JAS) phases of JS Niño. During the dissipation phase (OND) of JS Niño, a negative IOD-like pattern of weak SSTAs develops with corresponding surface wind anomalies (i.e., northwesterly) that are favorable for coastal downwelling along the Java–Sumatra coast. However, as discussed earlier, due to the weakening of the southeasterly

monsoonal wind and the associated deepening of the coastal thermocline after JAS (supplementary Fig. 6), the anomalous northwesterly winds along the Java–Sumatra coast in OND do not produce a pronounced JS Niño event.

Unlike La Niña, a robust pattern of downwelling favorable surface wind anomalies emerges along the equatorial and southeastern equatorial Indian Ocean during the onset phase of the double-peak JS Niño variety (Fig. 8d). As a result, the thermocline is deeper from the south coast of Java to the northeast equatorial region off Sumatra and shallower immediately southwest of the Java–Sumatra coast. Also during this early period (AMJ), warm SSTAs already prevail widely across the tropical Indian Ocean including in the southeastern equatorial region. The early season warm SSTAs are the residual of preseason warming, forced remotely during the dissipation phase of El Niño in boreal winter and spring (Fig. 4g). These surface wind and thermocline depth anomalies and the warm SSTAs along the Java–Sumatra coast intensify during the peak phase (Fig. 8e). This suggests that local Bjerknes feedback still plays an active role in the double-peak JS Niño variety, given that the remote influence of La Niña is generally weak during the onset and peak phases of JS Niño (Figs. 8a,b). Consistently, some double-peak JS Niño events occurred under a near-neutral ENSO condition in JAS. For instance, the 2016 JS Niño event, which is the strongest warm event during 1949–2019, occurred under a very weak and short-lived La Niña event and brought extremely high rainfall over Indonesia and Australia in June–September (Lim and Hendon 2017) (supplementary Figs. 2 and 5). During the dissipation phase of the double-peak JS Niño variety, warm SSTAs off the Java–Sumatra coast quickly diminish, while the anomalous patterns of surface winds and thermocline depth further intensify and propagate (or expand) westward (Fig. 8f). Additionally, cold SSTAs develop in the central tropical south Indian Ocean south of 10°S. It is likely that these atmosphere–ocean anomalies in OND are, to a certain extent, enhanced by La Niña through a strengthened Walker cell in the tropical Indian Ocean and the associated anomalous wind stress curl and Ekman pumping.

Similar to the double-peak JS Niño variety, during the onset phase of the on-season JS Niño variety, downwelling favorable surface wind anomalies appear along the equatorial and southeastern equatorial Indian Ocean (Fig. 8g). Although weak, warm SSTAs also appear along the south coast of Java. During the peak phase of the on-season JS Niño variety, the anomalous surface winds intensify; thus, the thermocline is deeper along the Java–Sumatra coast and shallower in the central tropical south Indian Ocean (Fig. 8h). The anomalous SSTs and surface winds quickly diminish during the dissipation phase since the seasonal mean atmosphere–ocean conditions along the Java–Sumatra coast become unfavorable for local Bjerknes feedback in OND (supplementary Fig. 6).

4. Discussion

a. What triggers local Bjerknes feedback?

It is widely accepted that ENSO is an important forcing mechanism for the IOD (e.g., Shinoda et al. 2004; Behera et al. 2006; Hong et al. 2008b; Yang et al. 2015; Zhang et al. 2015; Stuecker et al. 2017), which tends to peak in October (Saji et al. 1999). However, as shown and discussed in this study, during the onset phase of JSN (AMJ), the remote influence of ENSO is generally not robust enough to directly force the development of JSN. Thus, for most of the leading JSN varieties (i.e., the on-season JS Niña/Niño, double-peak JS Niño, and persistent JS Niña varieties), local Bjerknes feedback (Li et al. 2003) is a key ingredient for their emergence. However, it should be noted that JSN does not display any dominant frequency of oscillation (supplementary Fig. 7). This strongly suggests that JSN is not a self-sustained oscillation but a weakly damped oscillation, which by definition requires a finite amplitude perturbation to trigger and sustain the local Bjerknes feedback (Li et al. 2003).

Previous studies suggested that westward propagating oceanic Rossby waves across the equatorial south Indian Ocean could directly affect atmospheric convection in the western equatorial region to produce the IOD (e.g., Luo et al. 2008; Du et al. 2020). The oceanic Rossby waves may also reflect from the western boundary to produce eastward propagating equatorial Kelvin waves. These oceanic waves may further disturb the Wyrtki jets, the eastward flowing ocean currents along the equatorial Indian Ocean appearing in boreal spring and fall, and thus potentially trigger the IOD (e.g., Vinayachandran et al. 1999, 2007; Murtugudde et al. 2000; Han et al. 2004; Nagura and McPhaden 2010; Chakravorty et al. 2014; Zhang et al. 2014; McPhaden et al. 2015; Duan et al. 2016; Lim and Hendon 2017; Pujiana and McPhaden 2020). In line with these hypotheses, during the onset phase of the double-peak JS Niño variety, the thermocline across the Seychelles Dome in the southwestern tropical Indian Ocean is deeper (Fig. 8d). The deepened thermocline is remotely forced from the Pacific during the preseason (Xie et al. 2002; Rao and Behera 2005; Yu et al. 2005; Tozuka et al. 2010) (Fig. 4g). It is possible that the anomaly later propagates to the west and reflects from the western boundary to produce eastward propagating equatorial Kelvin waves, initiating local Bjerknes feedback that kick-starts the second peak. It is also possible that the residual of warm SSTAs in the southeastern tropical Indian Ocean formed during the preseason may persist and enhance the local Bjerknes feedback (Fig. 8d). However, in some cases the preseason anomalies completely dissipate before boreal summer (i.e., the preseason JS Niño/Niña variety). In addition, there are little-to-no preseason anomalies for the on-season JS Niña/Niña variety or the persistent JS Niña variety. Therefore, further study is needed to understand the extent to which the preseason anomalies of thermocline depth and SSTs can actually trigger the local Bjerknes feedback.

Other proposed onset mechanisms of the IOD involve subseasonal atmospheric processes, such as the Madden–Julian oscillation and boreal summer intraseasonal oscillation (e.g., Rao and Yamagata 2004; Rao et al. 2009; Weller et al. 2014; Zhang et al. 2021), a delayed response to the Pacific ENSO through the Indonesian Throughflow (e.g., Susanto et al. 2001; Yuan et al. 2011), recharge oscillator (McPhaden and Nagura 2014) and interhemispheric sea level pressure gradient (Lu and Ren 2020). Yet, some other studies point to atmosphere–ocean anomalies originating from the subtropical

south Indian Ocean as a potential driver of the IOD (e.g., Fischer et al. 2005; Y.-L. Zhang et al. 2020; Huang et al. 2021). In agreement with this hypothesis, prior to the onset phase of the persistent and on-season JS Niña varieties, an anticyclonic sea level pressure anomaly appears over the subtropical south Indian Ocean in March (supplementary Figs. 8a,d). This sea level pressure anomaly slowly shifts (or expands) toward the equator, producing anomalous southeasterly winds off the Java–Sumatra coast as early as April (supplementary Figs. 8b,e). This may in turn serve as a trigger for local Bjerknes feedback. Similarly, prior to the onset phase of the double-peak and on-season JS Niño varieties, a cyclonic sea level pressure anomaly forms over the subtropical south Indian Ocean and then slowly migrates toward the equator (supplementary Figs. 8g–l). Further study is needed to understand how these subtropical sea level pressure anomalies form and migrate equatorward.

b. *Relationship between JSN, IOB mode, and IOD*

The appearance of preseason warm/cold SSTAs along the Java–Sumatra coast, associated with the preseason and double-peak JSN varieties, is clearly tied to the IOB mode that is largely modulated by ENSO during its dissipation phase in boreal winter and spring. However, the relationship between JSN and the IOD in boreal summer and fall differs considerably, depending on how we define the IOD. For instance, we may identify an IOD event whenever significant SSTAs appear in the southeastern equatorial Indian Ocean, the western equatorial Indian Ocean, or both the southeastern and western equatorial Indian Oceans as long as the difference between them (i.e., DMI) is significantly different from zero. Under such a broad definition of the IOD, JSN is simply a subset of the IOD, by definition.

However, many of the IOD events identified in this way are not "dipoles." Therefore, an alternative way, which is used implicitly throughout this study, is to identify an IOD event only when an actual "dipole" occurs (i.e., significant SSTAs in both the southeastern and western equatorial Indian Oceans with opposite signs). Under this narrower definition of the IOD, some JSN events can be characterized as "dipole" and others as either "monopole" or "tripole." Specifically, the correlation coefficient of SSTAs between the western and southeastern equatorial Indian Oceans is only −0.10 during the peak season of JSN (JAS), indicating that JSN events are rarely characterized as "dipole" during their peak season. Additionally, although some JSN events may be characterized as "dipole" in boreal summer, a large portion of JSN events quickly dissipates after their peaks in JAS. Therefore, only some strong JS Niña events (i.e., the persistent JS Niña variety) persist throughout SON, the peak season of the IOD.

The weak correlation of SSTAs between the western and southeastern equational Indian Oceans becomes more evident if the ENSO signal is removed using a partial correlation analysis (supplementary Table 5). Note that this result is in agreement with the findings from Zhao and Nigam (2015), but in disagreement with Yamagata et al. (2003). The correlation of SSTAs between the western and southeastern equatorial Indian Ocean is mostly positive, except in boreal summer and fall, with a maximum negative correlation coefficient of −0.29 in SON. If the ENSO signal is removed, it becomes only −0.16, which is insignificant at the 95% confidence level. In contrast, the partial correlation of SSTAs between the western equatorial Indian Ocean and Niño-3.4 region (removing the influence of the southeastern equatorial Indian Ocean) is positive and significant at the 95% confidence level in all seasons, with a maximum correlation coefficient of 0.6 in OND. This suggests that SSTAs in the western equatorial Indian Ocean are, to a large extent, driven by the ENSO signal in all seasons and especially in OND. It is also interesting to note that the partial correlation of SSTAs between the southeastern equatorial Indian Ocean and Niño-3.4 region is relatively small in boreal summer and fall, with a maximum negative correlation coefficient of only −0.24 in ASO, which is barely significant at the 95% confidence level. This suggests that SSTAs in the southeastern equatorial Indian Ocean (i.e., JSN) are largely independent of the ENSO signal in boreal summer and fall.

In summary, the partial correlation analysis shows that SSTAs in the western and southeastern equatorial Indian Oceans are uncorrelated in boreal summer and fall, especially if the ENSO signal is removed. It also suggests that SSTAs in the western equatorial Indian Ocean are largely driven by the ENSO signal, particularly in OND, whereas SSTAs in the southeastern equatorial Indian Ocean are largely independent of the ENSO signal. These results from the partial correlation analysis suggest that the IOD is not triggered by a single mechanism, but rather a combined effect of two largely independent processes: local Bjerknes feedback in the southeastern equatorial Indian Ocean (i.e., JSN) and ENSO-induced SSTAs in the western equatorial Indian Ocean. The former tends to peak in JAS, and the latter in OND.

5. Summary and conclusions

To better understand atmosphere–ocean variability in the tropical Indian Ocean, here we explore JSN and its spatiotemporal diversity, associated regional rainfall variability, and onset mechanisms. JSN is largely associated with anomalous upwelling/downwelling along the Java–Sumatra coast and thus is closely phase-locked to the seasonal cycle, prevailing in JAS when the monsoonal winds are upwelling favorable along the Java–Sumatra coast. At times, JSN appears as a precursor to the IOD, which becomes mature in October (Saji et al. 1999), but JSN often occurs without corresponding SSTAs in the western equatorial Indian Ocean. JSN is essentially an intrinsic mode of variability driven by local Bjerknes feedback and thus does not rely on remote forcing from the Pacific for its emergence. However, the timing, zonal pattern, and amplitude of onset, peak, and dissipation are quite different from event to event.

Some JSN events first appear in the preseason (JFM) largely in response to the ENSO-induced IOB mode and then, after a short pause, reorganize in JAS (the double-peak JS Niño/Niña variety). Although these JSN events do not rely

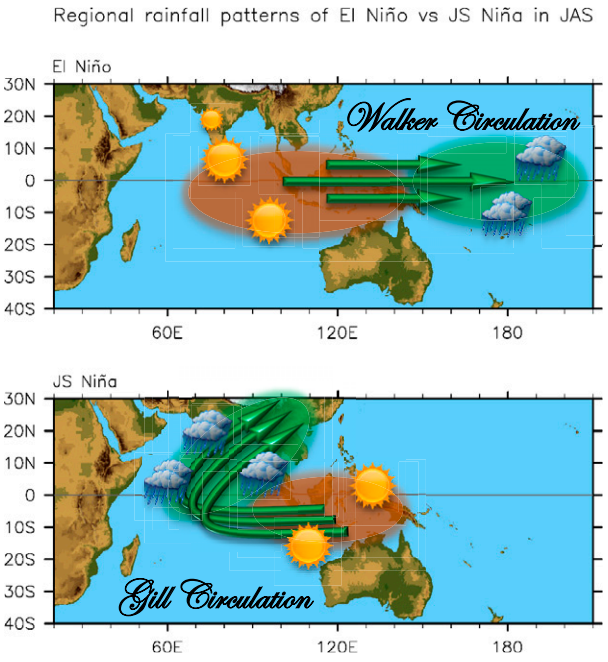

FIG. 9. A summary schematic of the precipitation (shading) and low-level wind anomalies (arrows) associated with (top) El Niño and (bottom) JS Niña in JAS. Brown and green shades represent decreased and increased precipitation, respectively. The double-peak JS Niña/Niño variety is often linked to El Niño/La Niña and the associated zonal seesaw pattern of rainfall anomalies with decreased rainfall over the Maritime Continent extending to India and increased rainfall in the western tropical Pacific, forced by ENSO-induced changes in the Pacific Walker cell. In contrast, the persistent and on-season JS Niña varieties produce a meridional seesaw pattern of rainfall anomalies that projects onto the South and Southeast Asian summer monsoons, driven by a Gill-type cross-hemispheric atmospheric circulation in response to the cold SSTAs along the Java–Sumatra coast.

on ENSO for their second peak in JAS, they are often linked to a specific flavor of La Niña/El Niño that transitions to the opposite phase and then intensifies during boreal summer and fall. Therefore, the associated regional rainfall pattern is greatly modulated by ENSO through changes in the Pacific Walker cell (Fig. 9a). In contrast, some JS Niña events appear predominantly in JAS (the on-season and persistent JS Niña varieties) and produce a meridional seesaw pattern of rainfall anomalies that projects onto the South and Southeast Asian summer monsoons. This pattern of rainfall anomalies is driven by a Gill-type cross-hemispheric atmospheric circulation in response to the cold SSTAs along the Java–Sumatra coast (Fig. 9b). Some of those JS Niña events are much stronger than others and display a strong positive IOD signature (the persistent JS Niña variety). These persistent JS Niña events (e.g., the 2019 JS Niña) potentially enhance—and are enhanced by—warm SSTAs in the neighboring regions of the tropical Indian and Pacific Oceans. They thus tend to persist longer throughout SON and produce particularly strong rainfall anomalies over the surrounding continents.

As summarized in Table 1, the main results presented in this study indicate that JSN develops earlier than the IOD as either a monopole, dipole or even tripole. JSN does not rely on ENSO for its emergence, and it is also an important driver of climate variability over the tropical Indian Ocean and the surrounding continents. Given these new findings, further analysis and modeling studies of JSN are warranted to better understand and monitor the atmosphere–ocean processes involved in the onset, peak and dissipation of JSN. These advances will likely lead to an earlier warning of extreme rainfall and flooding events in the most heavily populated areas of the world.

Acknowledgments. The authors acknowledge Yuko Okumura and three anonymous reviewers for insightful comments and suggestions, and Marlos Goes for reviewing the manuscript. This work was supported by the base funding of NOAA's Atlantic Oceanographic and Meteorological Laboratory (AOML), and by NOAA's Climate Program Office's Modeling, Analysis, Predictions, and Projections program (NA19OAR4310282), and NOAA's Weather Program Office. D.K., K.P., D.L.V., and S.C. were supported by NOAA's AOML in part under the auspices of the Cooperative Institute for Marine and Atmospheric Studies (CIMAS),

TABLE 1. JSN vs IOD. This summary table compares JSN and IOD with respect to their mature seasons, zonal patterns of SSTAs, driving mechanisms, rainfall patterns, rainfall mechanisms, and indices.

Terms	JSN	IOD
Mature season (month)	July–September	September–November (October)
Zonal pattern of SSTAs	Monopole, dipole, or tripole	Always dipole
Driving mechanism	Local Bjerknes feedback	ENSO-induced remote forcing and local Bjerknes feedback
Rainfall pattern	JAS: a meridional seesaw pattern of rainfall anomalies that projects on the South–Southeast Asian summer monsoons	SON: a zonal tripole pattern of rainfall anomalies between eastern Africa, the Maritime Continent, and the western tropical Pacific
Rainfall mechanism	Cross-hemispheric Gill-type circulation	Indo-Pacific Walker cells
Index	JSN index: SSTAs averaged in the Java and Sumatra coastal regions (9° and 3°S, 95°–105°E and 12° and 6°S, 105°–115°E)	DMI: gradient of SSTAs from the southeastern (90°–110°E and 10°S–0°) to the western equatorial Indian Ocean (50°–70°E and 10°S–10°N)

a cooperative institute of the University of Miami and NOAA, cooperative agreement NA20OAR4320472. E.L. was supported by the Australian Government's National Environmental Science Program.

Data availability statement. All data used in this paper are publicly available to download. The Centennial In Situ Observation-Based Estimates of the variability of SST are provided by the NOAA/Physical Sciences Division (PSD) at https://psl.noaa.gov/data/gridded/data.cobe.html. The NCEP–NCAR reanalysis is provided by the NOAA/PSD at https://psl.noaa.gov/data/gridded/data.ncep.reanalysis.derived.html. NOAA's precipitation reconstruction dataset is provided by the NOAA/PSD at https://psl.noaa.gov/data/gridded/data.prec.html. The European Centre for Medium-Range Weather Forecasts Ocean Reanalysis System 5 dataset is available through the Copernicus Marine Environment Monitoring Service data portal at https://icdc.cen.uni-hamburg.de/daten/reanalysis-ocean/easy-init-ocean/ecmwf-oras5.html.

REFERENCES

Abram, N. J., M. K. Gagan, M. T. McCulloch, J. Chappell, and W. S. Hantoro, 2003: Coral reef death during the 1997 Indian Ocean dipole linked to Indonesian wildfires. *Science*, **301**, 952–955, https://doi.org/10.1126/science.1083841.

Allan, R. J., and Coauthors, 2001: Is there an Indian Ocean dipole and is it independent of the El Niño–Southern Oscillation? *CLIVAR Exchanges*, No. 6, International CLIVAR Project Office, Southampton, United Kingdom, 18–22.

Ashok, K., Z. Guan, and T. Yamagata, 2001: Impact of the Indian Ocean dipole on the relationship between the Indian monsoon rainfall and ENSO. *Geophys. Res. Lett.*, **28**, 4499–4502, https://doi.org/10.1029/2001GL013294.

——, ——, N. H. Saji, and T. Yamagata, 2004: Individual and combined influences of ENSO and the Indian Ocean dipole on the Indian summer monsoon. *J. Climate*, **17**, 3141–3155, https://doi.org/10.1175/1520-0442(2004)017<3141:IACIOE>2.0.CO;2.

Behera, S. K., J. J. Luo, S. Masson, S. A. Rao, H. Sakuma, and T. Yamagata, 2006: A CGCM study on the interaction between IOD and ENSO. *J. Climate*, **19**, 1688–1705, https://doi.org/10.1175/JCLI3797.1.

Cai, W., and Y. Qiu, 2013: An observation-based assessment of nonlinear feedback processes associated with the Indian Ocean dipole. *J. Climate*, **26**, 2880–2890, https://doi.org/10.1175/JCLI-D-12-00483.1.

——, P. van Rensch, T. Cowan, and H. H. Hendon, 2011: Teleconnection pathways of ENSO and the IOD and the mechanisms for impacts on Australian rainfall. *J. Climate*, **24**, 3910–3923, https://doi.org/10.1175/2011JCLI4129.1.

Chakravorty, S., C. Gnanaseelan, J. S. Chowdary, and J.-J. Luo, 2014: Relative role of El Niño and IOD forcing on the southern tropical Indian Ocean Rossby waves. *J. Geophys. Res. Oceans*, **119**, 5105–5122, https://doi.org/10.1002/2013JC009713.

Chen, M., P. Xie, J. E. Janowiak, and P. A. Arkin, 2002: Global land precipitation: A 50-yr monthly analysis based on gauge observations. *J. Hydrometeor.*, **3**, 249–266, https://doi.org/10.1175/1525-7541(2002)003<0249:GLPAYM>2.0.CO;2.

Dommenget, D., 2011: An objective analysis of the observed spatial structure of the tropical Indian Ocean SST variability. *Climate Dyn.*, **36**, 2129–2145, https://doi.org/10.1007/s00382-010-0787-1.

Du, Y., T. Qu, and G. Meyers, 2008: Interannual variability of sea surface temperature off Java and Sumatra in a global GCM. *J. Climate*, **21**, 2451–2465, https://doi.org/10.1175/2007JCLI1753.1.

——, W. Cai, and Y. Wu, 2013: A new type of the Indian Ocean dipole since the mid-1970s. *J. Climate*, **26**, 959–972, https://doi.org/10.1175/JCLI-D-12-00047.1.

——, Y. Zhang, L.-Y. Zhang, T. Tozuka, B. Ng, and W. Cai, 2020: Thermocline warming induced extreme Indian Ocean dipole in 2019. *Geophys. Res. Lett.*, **47**, e2020GL090079, https://doi.org/10.1029/2020GL090079.

Duan, Y., L. Liu, G. Han, H. Liu, W. Yu, and G. Yan, 2016: Anomalous behaviors of Wyrtki jets in the equatorial Indian Ocean during 2013. *Sci. Rep.*, **6**, 29688, https://doi.org/10.1038/srep29688.

Endo, S., and T. Tozuka, 2016: Two flavors of the Indian Ocean dipole. *Climate Dyn.*, **46**, 3371–3385, https://doi.org/10.1007/s00382-015-2773-0.

England, M. H., C. C. Ummenhofer, and A. Santoso, 2006: Interannual rainfall extremes over southwest western Australia linked to Indian Ocean climate variability. *J. Climate*, **19**, 1948–1969, https://doi.org/10.1175/JCLI3700.1.

Fischer, A. S., P. Terray, E. Guilyardi, S. Gualdi, and P. Delecluse, 2005: Two independent triggers for the Indian Ocean dipole/zonal mode in a coupled GCM. *J. Climate*, **18**, 3428–3449, https://doi.org/10.1175/JCLI3478.1.

Gill, A. E., 1980: Some simple solutions for heat-induced tropical circulation. *Quart. J. Roy. Meteor. Soc.*, **106**, 447–462, https://doi.org/10.1002/qj.49710644905.

Han, W., P. Webster, R. Lukas, P. Hacker, and A. Hu, 2004: Impact of atmospheric intraseasonal variability in the Indian Ocean: Low-frequency rectification in equatorial surface current and transport. *J. Phys. Oceanogr.*, **34**, 1350–1372, https://doi.org/10.1175/1520-0485(2004)034<1350:IOAIVI>2.0.CO;2.

——, J. Vialard, M. J. McPhaden, T. Lee, Y. Masumoto, M. Feng, and W. P. de Ruijter, 2014: Indian Ocean decadal variability: A review. *Bull. Amer. Meteor. Soc.*, **95**, 1679–1703, https://doi.org/10.1175/BAMS-D-13-00028.1.

Hastenrath, S., 2002: Dipoles, temperature gradients, and tropical climate anomalies. *Bull. Amer. Meteor. Soc.*, **83**, 735–738, https://doi.org/10.1175/1520-0477(2002)083<0735:WLACNM>2.3.CO;2.

Hendon, H. H., E. Lim, and G. Liu, 2012: The role of air–sea interaction for prediction of Australian summer monsoon rainfall. *J. Climate*, **25**, 1278–1290, https://doi.org/10.1175/JCLI-D-11-00125.1.

Hong, C.-C., T. Li, and J.-S. Kug, 2008a: Asymmetry of the Indian Ocean dipole. Part I: Observational analysis. *J. Climate*, **21**, 4834–4848, https://doi.org/10.1175/2008JCLI2222.1.

——, M.-M. Lu, and M. Kanamitsu, 2008b: Temporal and spatial characteristics of positive and negative Indian Ocean dipole with and without ENSO. *J. Geophys. Res.*, **113**, D08107, https://doi.org/10.1029/2007JD009151.

Huang, B., T. Su, S. Qu, H. Zhang, S. Hu, and G. Feng, 2021: Strengthened relationship between tropical Indian Ocean dipole and subtropical Indian Ocean dipole after the late 2000s. *Geophys. Res. Lett.*, **48**, e2021GL094835, https://doi.org/10.1029/2021GL094835.

Ishii, M., A. Shouji, S. Sugimoto, and T. Matsumoto, 2005: Objective analyses of sea-surface temperature and marine meteorological variables for the 20th century using ICOADS and the Kobe collection. *Int. J. Climatol.*, **25**, 865–879, https://doi.org/10.1002/joc.1169.

Izumo, T., and Coauthors, 2010: Influence of the state of the Indian Ocean dipole on the following year's El Niño. *Nat. Geosci.*, **3**, 168–172, https://doi.org/10.1038/ngeo760.

Kalnay, E., and Coauthors, 1996: The NCEP/NCAR 40-Year Reanalysis Project. *Bull. Amer. Meteor. Soc.*, **77**, 437–471, https://doi.org/10.1175/1520-0477(1996)077<0437:TNYRP>2.0.CO;2.

Kumar, K. K., B. Rajagopalan, M. Hoerling, G. Bates, and M. Cane, 2006: Unraveling the mystery of Indian monsoon failure during El Niño. *Science*, **314**, 115–119, https://doi.org/10.1126/science.1131152.

Lee, S.-K., P. N. DiNezio, E.-S. Chung, S.-W. Yeh, A. T. Wittenberg, and C. Wang, 2014: Spring persistence, transition, and resurgence of El Niño. *Geophys. Res. Lett.*, **41**, 8578–8585, https://doi.org/10.1002/2014GL062484.

——, H. Lopez, E.-S. Chung, P. N. DiNezio, S.-W. Yeh, and A. T. Wittenberg, 2018: On the fragile relationship between El Niño and California rainfall. *Geophys. Res. Lett.*, **45**, 907–915, https://doi.org/10.1002/2017GL076197.

Li, T., B. Wang, C.-P. Chang, and Y. Zhang, 2003: A theory for the Indian Ocean dipole–zonal mode. *J. Atmos. Sci.*, **60**, 2119–2135, https://doi.org/10.1175/1520-0469(2003)060<2119:ATFTIO>2.0.CO;2.

Lim, E.-P., and H. H. Hendon, 2017: Causes and predictability of the negative Indian Ocean dipole and its impact on La Niña during 2016. *Sci. Rep.*, **7**, 12619, https://doi.org/10.1038/s41598-017-12674-z.

——, ——, M. Zhao, and Y. Yin, 2017: Inter-decadal variations in the linkages between ENSO, the IOD and south-eastern Australian springtime rainfall in the past 30 years. *Climate Dyn.*, **49**, 97–112, https://doi.org/10.1007/s00382-016-3328-8.

——, and Coauthors, 2021: The 2019 Southern Hemisphere stratospheric polar vortex weakening and its impacts. *Bull. Amer. Meteor. Soc.*, **102**, E1150–E1171, https://doi.org/10.1175/BAMS-D-20-0112.1.

Lu, B., and H.-L. Ren, 2020: What caused the extreme Indian Ocean dipole event in 2019? *Geophys. Res. Lett.*, **47**, e2020GL087768, https://doi.org/10.1029/2020GL087768.

Luo, J.-J., S. K. Behera, Y. Masumoto, H. Sakuma, and T. Yamagata, 2008: Successful prediction of the consecutive IOD in 2006 and 2007. *Geophys. Res. Lett.*, **35**, L14S02, https://doi.org/10.1029/2007GL032793.

——, R. Zhang, S. K. Behera, Y. Masumoto, F.-F. Jin, R. Lukas, and T. Yamagata, 2010: Interaction between El Niño and extreme Indian Ocean dipole. *J. Climate*, **23**, 726–742, https://doi.org/10.1175/2009JCLI3104.1.

McPhaden, M. J., and M. Nagura, 2014: Indian Ocean dipole interpreted in terms of recharge oscillator theory. *Climate Dyn.*, **42**, 1569–1586, https://doi.org/10.1007/s00382-013-1765-1.

——, Y. Wang, and M. Ravichandran, 2015: Volume transports of the Wyrtki jets and their relationship to the Indian Ocean dipole. *J. Geophys. Res. Oceans*, **120**, 5302–5317, https://doi.org/10.1002/2015JC010901.

Meyers, G., P. McIntosh, L. Pigot, and M. Pook, 2007: The years of El Niño, La Niña, and interactions with the tropical Indian Ocean. *J. Climate*, **20**, 2872–2880, https://doi.org/10.1175/JCLI4152.1.

Murtugudde, R., J. P. McCreary, and A. J. Busalacchi, 2000: Oceanic processes associated with anomalous events in the Indian Ocean with relevance to 1997–1998. *J. Geophys. Res.*, **105**, 3295–3306, https://doi.org/10.1029/1999JC900294.

Nagura, M., and M. J. McPhaden, 2010: Dynamics of zonal current variations associated with the Indian Ocean dipole. *J. Geophys. Res.*, **115**, C11026, https://doi.org/10.1029/2010JC006423.

North, G. R., T. L. Bell, R. F. Cahalan, and F. J. Moeng, 1982: Sampling errors in the estimation of empirical orthogonal functions. *Mon. Wea. Rev.*, **110**, 699–706, https://doi.org/10.1175/1520-0493(1982)110<0699:SEITEO>2.0.CO;2.

Pujiana, K., and M. J. McPhaden, 2020: Intraseasonal Kelvin waves in the equatorial Indian Ocean and their propagation into the Indonesian seas. *J. Geophys. Res. Oceans*, **125**, e2019JC015839, https://doi.org/10.1029/2019JC015839.

Rao, S. A., and T. Yamagata, 2004: Abrupt termination of Indian Ocean dipole events in response to intraseasonal disturbances. *Geophys. Res. Lett.*, **31**, L19306, https://doi.org/10.1029/2004GL020842.

——, and S. K. Behera, 2005: Subsurface influence on SST in the tropical Indian Ocean: Structure and interannual variability. *Dyn. Atmos. Oceans*, **39**, 103–135, https://doi.org/10.1016/j.dynatmoce.2004.10.014.

——, J.-J. Luo, S. K. Behera, and T. Yamagata, 2009: Generation and termination of Indian Ocean dipole events in 2003, 2006 and 2007. *Climate Dyn.*, **33**, 751–767, https://doi.org/10.1007/s00382-008-0498-z.

Ratna, S. B., A. Cherchi, T. J. Osborn, M. Joshi, and U. Uppara, 2020: The extreme positive Indian Ocean dipole of 2019 and associated Indian summer monsoon rainfall response. *Geophys. Res. Lett.*, **47**, e2020GL091497, https://doi.org/10.1029/2020GL091497.

Risbey, J. S., M. J. Pook, P. C. McIntosh, M. C. Wheeler, and H. H. Hendon, 2009: On the remote drivers of rainfall variability in Australia. *Mon. Wea. Rev.*, **137**, 3233–3253, https://doi.org/10.1175/2009MWR2861.1.

Saji, N. H., B. N. Goswami, P. N. Vinayachandran, and T. Yamagata, 1999: A dipole mode in the tropical Indian Ocean. *Nature*, **401**, 360–363, https://doi.org/10.1038/43854.

Shinoda, T., H. H. Hendon, and M. A. Alexander, 2004: Surface and subsurface dipole variability in the Indian Ocean and its relation with ENSO. *Deep-Sea Res. I*, **51**, 619–635, https://doi.org/10.1016/j.dsr.2004.01.005.

Sreelekha, P. N., and C. A. Babu, 2019: Is the negative IOD during 2016 the reason for monsoon failure over southwest peninsular India? *Meteor. Atmos. Phys.*, **131**, 413–420, https://doi.org/10.1007/s00703-017-0574-1.

Srivastava, A. K., J. V. Revadekar, and M. Rajeevan, 2020: South Asia [in "State of the Climate in 2019"]. *Bull. Amer. Meteor. Soc.*, **101** (8), S394–S397, https://doi.org/10.1175/2020BAMSStateoftheClimate_Chapter7.1.

Stuecker, M. F., A. Timmermann, F.-F. Jin, Y. Chikamoto, W. Zhang, A. T. Wittenberg, E. Widiasih, and S. Zhao, 2017: Revisiting ENSO/Indian Ocean dipole phase relationships. *Geophys. Res. Lett.*, **44**, 2481–2492, https://doi.org/10.1002/2016GL072308.

Sun, S., J. Lan, Y. Fang, and X. Gao, 2015: A triggering mechanism for the Indian Ocean dipoles independent of ENSO. *J. Climate*, **28**, 5063–5076, https://doi.org/10.1175/JCLI-D-14-00580.1.

Susanto, R. D., A. L. Gordon, and Q. Zheng, 2001: Upwelling along the coasts of Java and Sumatra and its relation to ENSO. *Geophys. Res. Lett.*, **28**, 1599–1602, https://doi.org/10.1029/2000GL011844.

Tobin, S., and C. Ganter, 2020: Australia [in "State of the Climate in 2019"]. *Bull. Amer. Meteor. Soc.*, **101** (8), S405–S409, https://doi.org/10.1175/2020BAMSStateoftheClimate_Chapter7.1.

Tozuka, T., T. Yokoi, and T. Yamagata, 2010: A modeling study of interannual variations of the Seychelles Dome. *J. Geophys. Res.*, **115**, C04005, https://doi.org/10.1029/2009JC005547.

Vallès-Casanova, I., S.-K. Lee, G. R. Foltz, and J. L. Pelegrí, 2020: On the spatiotemporal diversity of Atlantic Niño and associated rainfall variability over West Africa and South America. *Geophys. Res. Lett.*, **47**, e2020GL087108, https://doi.org/10.1029/2020GL087108.

Vinayachandran, P. N., N. H. Saji, and T. Yamagata, 1999: Response of the equatorial Indian Ocean to an unusual wind event during 1994. *Geophys. Res. Lett.*, **26**, 1613–1616, https://doi.org/10.1029/1999GL900179.

——, J. Kurian, and C. P. Neema, 2007: Indian Ocean response to anomalous conditions in 2006. *Geophys. Res. Lett.*, **34**, L15602, https://doi.org/10.1029/2007GL030194.

Wang, G., W. Cai, K. Yang, A. Santoso, and T. Yamagata, 2020: A unique feature of the 2019 extreme positive Indian Ocean dipole event. *Geophys. Res. Lett.*, **47**, e2020GL088615, https://doi.org/10.1029/2020GL088615.

Webster, P. J., A. M. Moore, J. P. Loschnigg, and R. R. Leben, 1999: Coupled ocean-atmosphere dynamics in the Indian Ocean during 1997–98. *Nature*, **401**, 356–360, https://doi.org/10.1038/43848.

Weller, E., W. Cai, Y. Du, and S.-K. Min, 2014: Differentiating flavors of the Indian Ocean dipole using dominant modes in tropical Indian Ocean rainfall. *Geophys. Res. Lett.*, **41**, 8978–8986, https://doi.org/10.1002/2014GL062459.

Wu, R., and B. P. Kirtman, 2004: Understanding the impacts of the Indian Ocean on ENSO variability in a coupled GCM. *J. Climate*, **17**, 4019–4031, https://doi.org/10.1175/1520-0442(2004)017<4019:UTIOTI>2.0.CO;2.

Xie, S., H. Annamalai, F. A. Schott, and J. P. McCreary Jr., 2002: Structure and mechanisms of south Indian Ocean climate variability. *J. Climate*, **15**, 864–878, https://doi.org/10.1175/1520-0442(2002)015<0864:SAMOSI>2.0.CO;2.

Yamagata, T., S. K. Behera, S. A. Rao, Z. Guan, K. Ashok, and H. N. Saji, 2003: Comments on "Dipoles, temperature gradients, and tropical climate anomalies." *Bull. Amer. Meteor. Soc.*, **84**, 1418–1422, https://doi.org/10.1175/BAMS-84-10-1415.

Yang, J., Q. Liu, S.-P. Xie, Z. Liu, and L. Wu, 2007: Impact of the Indian Ocean SST basin mode on the Asian summer monsoon. *Geophys. Res. Lett.*, **34**, L02708, https://doi.org/10.1029/2006GL028571.

Yang, Y., S.-P. Xie, L. Wu, Y. Kosaka, N. Lau, and G. A. Vecchi, 2015: Seasonality and predictability of the Indian Ocean dipole mode: ENSO forcing and internal variability. *J. Climate*, **28**, 8021–8036, https://doi.org/10.1175/JCLI-D-15-0078.1.

Yu, W., B. Xiang, L. Liu, and N. Liu, 2005: Understanding the origins of interannual thermocline variations in the tropical Indian Ocean. *Geophys. Res. Lett.*, **32**, L24706, https://doi.org/10.1029/2005GL024327.

Yuan, D., and Coauthors, 2011: Forcing of the Indian Ocean dipole on the interannual variations of the tropical Pacific Ocean: Roles of the Indonesian Throughflow. *J. Climate*, **24**, 3593–3608, https://doi.org/10.1175/2011JCLI3649.1.

Zhang, D., M. J. McPhaden, and T. Lee, 2014: Observed interannual variability of zonal currents in the equatorial Indian Ocean thermocline and their relation to Indian Ocean dipole. *Geophys. Res. Lett.*, **41**, 7933–7941, https://doi.org/10.1002/2014GL061449.

Zhang, L.-Y., Y. Du, W. Cai, Z. Chen, T. Tozuka, and J.-Y. Yu, 2020: Triggering the Indian Ocean dipole from the Southern Hemisphere. *Geophys. Res. Lett.*, **47**, e2020GL088648, https://doi.org/10.1029/2020GL088648.

——, W. Han, and Z.-Z. Hu, 2021: Inter-basin and multiple-time-scale interactions in generating the 2019 extreme Indian Ocean dipole. *J. Climate*, **34**, 4553–4566, https://doi.org/10.1175/JCLI-D-20-0760.1.

Zhang, W., Y. Wang, F.-F. Jin, M. F. Stuecker, and A. G. Turner, 2015: Impact of different El Niño types on the El Niño/IOD relationship. *Geophys. Res. Lett.*, **42**, 8570–8576, https://doi.org/10.1002/2015GL065703.

Zhang, Y., J. Li, S. Zhao, F. Zheng, J. Feng, Y. Li, and Y. Xu, 2020: Indian Ocean tripole mode and its associated atmospheric and oceanic processes. *Climate Dyn.*, **55**, 1367–1383, https://doi.org/10.1007/s00382-020-05331-1.

Zhao, M., and H. H. Hendon, 2009: Representation and prediction of the Indian Ocean dipole in the POAMA seasonal forecast model. *Quart. J. Roy. Meteor. Soc.*, **135**, 337–352, https://doi.org/10.1002/qj.370.

Zhao, Y., and S. Nigam, 2015: The Indian Ocean dipole: A monopole in SST. *J. Climate*, **28**, 3–19, https://doi.org/10.1175/JCLI-D-14-00047.1.

Zuo, H., M. A. Balmaseda, and K. Mogensen, 2017: The new eddy-permitting ORAP5 ocean reanalysis: Description, evaluation and uncertainties in climate signals. *Climate Dyn.*, **49**, 791–811, https://doi.org/10.1007/s00382-015-2675-1.